

# Seamless integration of the coastal ocean in global marine carbon cycle modeling

M. Mathis<sup>1</sup>, K. Logemann<sup>1</sup>, J. Maerz<sup>2</sup>, F. Lacroix<sup>3</sup>, S. Hagemann<sup>1</sup>, F. Chugini<sup>2</sup>, L. Ramme<sup>2,4</sup>, T. Ilyina<sup>2</sup>, P. Korn<sup>2</sup>, and C. Schrum<sup>5</sup>

<sup>1</sup>Helmholtz-Zentrum Hereon, Institute of Coastal Systems, Max-Planck-Str. 1, D-21502 Geesthacht

<sup>2</sup>Max-Planck-Institute for Meteorology, Bundesstr. 53, D-20146 Hamburg

<sup>3</sup>Max-Planck-Institute for Biogeochemistry, Hans-Knöll-Str. 10, D-07745 Jena

<sup>4</sup>International Max Planck Research School on Earth System Modelling, Hamburg, Germany

<sup>5</sup>University of Hamburg, Institute of Oceanography, Bundesstr. 53, D-20146 Hamburg

## Key Points:

- We introduce the first global ocean-biogeochemistry model with a dedicated representation of coastal carbon dynamics.
- We globally apply a grid refinement in the coastal ocean to better resolve regional circulation features, including ocean-shelf exchange.
- We explicitly incorporate key physical and biogeochemical processes controlling coastal carbon dynamics.

---

Corresponding author: Moritz Mathis, [moritz.mathis@hereon.de](mailto:moritz.mathis@hereon.de)

## Abstract

In this paper, we present the first global ocean-biogeochemistry model that uses a telescoping high resolution for an improved representation of coastal carbon dynamics: ICON-Coast. Based on the unstructured triangular grid topology of the model, we globally apply a grid refinement in the land-ocean transition zone to better resolve the complex circulation of shallow shelves and marginal seas as well as ocean-shelf exchange. Moreover, we incorporate tidal currents including bottom drag effects, and extend the parameterizations of the model's biogeochemistry component to account explicitly for key shelf-specific carbon transformation processes. These comprise sediment resuspension, temperature-dependent remineralization in the water column and sediment, riverine matter fluxes from land including terrestrial organic carbon, and variable sinking speed of aggregated particulate matter. The combination of regional grid refinement and enhanced process representation enables for the first time a seamless incorporation of the global coastal ocean in model-based Earth system research. In particular, ICON-Coast embraces all coastal areas around the globe within a single, consistent ocean-biogeochemistry model, thus naturally accounting for two-way coupling of ocean-shelf feedback mechanisms at the global scale. The high quality of the model results as well as the efficiency in computational cost and storage requirements proves this strategy a pioneering approach for global high-resolution modeling. We conclude that ICON-Coast represents a new tool to deepen our mechanistic understanding of the role of the land-ocean transition zone in the global carbon cycle, and to narrow related uncertainties in global future projections.

## Plain Language Summary

The coastal ocean, including shallow shelf and marginal seas, is a largely missing component of current global carbon budgeting. Yet, its capacity in carbon storage and transformation is crucial to be included in a science-based development of sustainable climate change mitigation and adaptation strategies. Global ocean-biogeochemistry models are powerful tools to investigate the marine carbon cycle of the open ocean. The coastal ocean, however, is poorly represented in global models to date, because of missing key processes controlling coastal carbon dynamics and too coarse grid resolutions to adequately resolve coastal circulation features. Here, we introduce the first global ocean-biogeochemistry model with a dedicated representation of the coastal ocean and associated marine carbon dynamics: ICON-Coast. In this model, we globally apply a grid refinement in the coastal ocean and account explicitly for various shelf-specific physical and biogeochemical processes. This approach enables for the first time a seamless incorporation of the global coastal ocean in model-based Earth system research. In particular, ICON-Coast represents a new tool to deepen our mechanistic understanding about the role of the land-ocean transition zone in the global carbon cycle, and to narrow related uncertainties in possible and plausible climate futures.

## 1 Introduction

Our current understanding about the role of the coastal ocean in the marine carbon cycle is limited and fragmentary. Considerable knowledge gaps are related to the interaction between the diverse sources and sinks of carbon in the highly heterogeneous and dynamic land-ocean transition zone and their relation to the biogeochemical processes in the open ocean (Regnier et al., 2013; Ward et al., 2017; G. G. Laruelle et al., 2018). Under present-day climatic conditions, the global coastal ocean has been identified as a net sink for atmospheric CO<sub>2</sub> (G. Laruelle et al., 2014; Gruber, 2015). However, to what extent coastal areas around the globe are taking up or releasing carbon, as well as how much of the carbon exported from the coastal areas enters the deep ocean, remains unclear (Bauer et al., 2013; Roobaert et al., 2019). The coastal ocean, thus, is a largely missing component of current global carbon budgeting (Fennel et al., 2019; Hauck et al., 2020), yet its capacity in

68 carbon storage and transformation is crucial to be included in a science-based development  
69 of sustainable mitigation and adaptation strategies to global climate change (Nellemann et  
70 al., 2009; Schmidt et al., 2017; Luisetti et al., 2020).

71 The general view is that in coastal areas of middle and high latitudes, net CO<sub>2</sub> draw-  
72 down at the sea surface is induced by high biological productivity and an efficient export of  
73 sequestered carbon to the adjacent deep open ocean, which outcompetes outgassing in low  
74 latitudes driven by temperature effects and substantial terrestrial carbon inputs (Borges &  
75 Frankignoulle, 2005; Cai, 2011). However, observation- and model-based estimates of the  
76 carbon fluxes across the boundaries of the coastal ocean, determining the overall budget, are  
77 poorly constrained. About 2 Gt C yr<sup>-1</sup> uncertainty is associated with the amount of carbon  
78 deposited in coastal sediments, with estimates ranging from 0.2-2.2 Gt C yr<sup>-1</sup> (Krumins et  
79 al., 2013). This is about the same amount taken up from the atmosphere by the entire  
80 global ocean at present (Park et al., 2010; Landschützer et al., 2016). About 1 Gt C yr<sup>-1</sup>  
81 uncertainty is associated with the coastal CO<sub>2</sub> flux at the air-sea interface, ranging from  
82 0.1-1.0 Gt C yr<sup>-1</sup> uptake (G. G. Laruelle et al., 2010; Bourgeois et al., 2016), although more  
83 recent studies point rather towards the lower end of this spread (Roobaert et al., 2019;  
84 Lacroix et al., 2021b). More accurate estimates of coastal carbon fluxes are thus also needed  
85 to robustly quantify the anthropogenic perturbation of the global carbon cycle, which is a  
86 key diagnostic of the evolution of climate change and the effectiveness of climate policies  
87 (Canadell et al., 2010; Friedlingstein et al., 2020).

88 Observations of processes relevant to constrain uncertainties in coastal carbon dynamics  
89 are methodologically challenging. Moreover, their spatial and temporal coverage is still  
90 scarce and often biased towards certain regions, latitudes and seasons (Painting et al., 2020;  
91 Ward et al., 2020). Recent studies applied machine learning algorithms to close data gaps by  
92 extrapolating collinearities between target and proxy observables (Lee et al., 2019; Gregor  
93 et al., 2019). The results, though, are often sensitive to the choice of the specific approach.

94 Global ocean-biogeochemistry models are powerful tools to gain understanding about  
95 the functioning of the marine carbon cycle and to test hypotheses about its response to  
96 future scenarios following various socio-economic climate policy directions. To investigate  
97 the coastal ocean, however, global ocean-biogeochemistry models are faced with conceptual  
98 limitations (Ward et al., 2020). First, global models are not designed to capture the var-  
99 ious energetic processes characterizing biogeochemical shelf sea dynamics such as a strong  
100 interaction between the water column and the sediment, strong internal mixing, or a strong  
101 influence of matter fluxes from land (Fig. 1). Many of these processes are thus typically  
102 underrepresented by global biogeochemistry models, if implemented at all (Allen et al.,  
103 2010; Hauck et al., 2020). And second, a comparatively high grid resolution is required to  
104 adequately resolve shelf-specific processes as well as ocean-shelf exchange. In the shallow  
105 coastal ocean, the horizontal grid resolution necessary to resolve the characteristic length  
106 scale of the ocean circulation ranges between 1/16° and 1/50° (Hallberg, 2013).

107 Setting up a global model with high grid resolution is not a problem in the first place  
108 (e.g. Cheng et al., 2016; Z. Li et al., 2017; Hewitt et al., 2020). The study of global carbon  
109 dynamics in the context of contemporary increasing atmospheric pCO<sub>2</sub>, however, requires  
110 simulation periods of at least multiple decades or even centuries, irrespective of still much  
111 longer spinup simulations needed to drive the physical and biogeochemical state of the  
112 ocean into equilibrium. Running a conventional global biogeochemistry model at the desired  
113 resolutions of 1/16° or higher for several decades, though, is too resource intensive under  
114 today's high-performance computing (HPC) capacities, thus excluding this application for  
115 practical reasons. Global ocean-biogeochemistry models contributing to the 6th phase of  
116 the Coupled Model Intercomparison Project (CMIP6), for example, were run with nominal  
117 horizontal resolutions of 1/2° to 1° (Séférian et al., 2020). Model-based investigations of the  
118 coastal ocean therefore have mainly pursued the application of regional model systems that  
119 enable both, specific process adaptation and finescale grid resolution at lower computational  
120 costs. Inconsistencies due to the prescribed forcing at the open lateral boundaries, however,

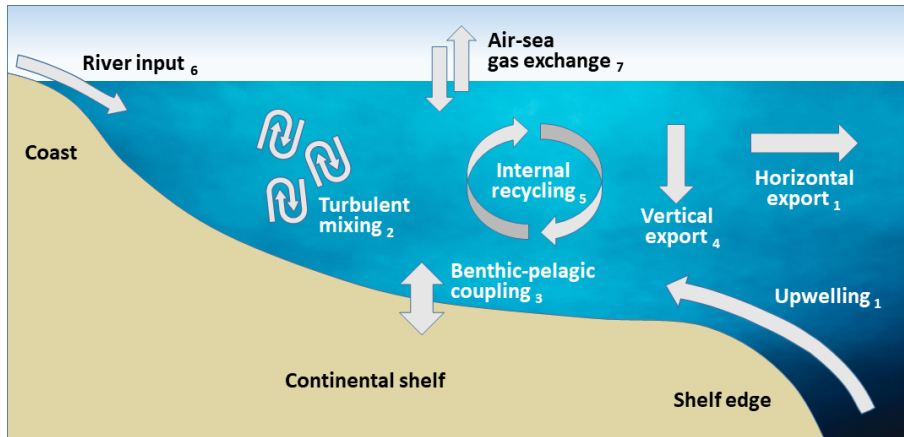


**Figure 1:** Schematic of key processes controlling coastal carbon dynamics. Attached indices are referred to in the results section 3

121 can lead to spurious artefacts influencing the model results in the interior of the regional  
 122 domain (Marsaleix et al., 2006; Z. Liu & Gan, 2016; Mathis et al., 2018). Moreover, global  
 123 budgeting of the coastal ocean requires global coastal coverage, which can hardly be obtained  
 124 by regional modeling efforts.

125 In this paper, we present the first global ocean-biogeochemistry model that overcomes  
 126 these technical barriers of inadequate grid resolution and process representation in the  
 127 coastal ocean. We build our development on the ocean component ICON-O of the new  
 128 Earth system model of the Max-Planck-Institute for Meteorology (MPI-Met) in Hamburg  
 129 and construct a subversion of this model with a dedicated focus on the land-ocean transi-  
 130 tion zone: ICON-Coast. For this task, we take advantage of the triangular grid structure  
 131 of ICON-O and globally apply a regional grid refinement in the coastal ocean. Logemann  
 132 et al. (2021) have demonstrated a significant improvement of coastal tidal amplitudes sim-  
 133 ulated with ICON-O when such a regional refinement is used. The advantages of installing  
 134 variable-resolution grids in global Earth system models to accommodate complex biogeo-  
 135 chemical interactions in the terrestrial-aquatic interface were recently emphasized by Ward  
 136 et al. (2020). And the use of unstructured grids was envisaged the most versatile, effi-  
 137 cient and elegant way to improve our understanding of the role of shelf seas in global-scale  
 138 processes already by Holt et al. (2009). In addition to the regional grid refinement, we  
 139 incorporate several modifications and extensions of the standard modules of ICON-O, in  
 140 particular for the biogeochemistry component HAMOCC, to improve the representation of  
 141 shelf-specific processes related to coastal carbon dynamics (Fig. 1).

142 The aim of this development is to provide a tool for reducing uncertainties in our un-  
 143 derstanding of the global carbon cycle and its governing processes via an improved modeling  
 144 approach. A seamless connection of the open and coastal ocean merged into a global ocean-  
 145 biogeochemistry model enables a consistent two-way coupling of cross-scale physical and  
 146 biogeochemical feedback mechanisms in all coastal regions of the world. To lay the grounds  
 147 for various scientific applications, we here introduce the general concept of ICON-Coast and  
 148 exemplify the skills and potentials of the model by showing results of simulated physical and  
 149 biogeochemical key processes related to coastal carbon dynamics.

## 2 Methods

### 2.1 Model description of ICON-O

The basis of our development is the ocean-sea ice-biogeochemistry model of the MPI-Met in Hamburg, ICON-O (Korn, 2017; Korn & Linardakis, 2018; Logemann et al., 2021). The physical core of the model is based on finite volume numerics. The grid structure discretizes the spherical surface of the global ocean by triangular cells with a C-type staggering of variables. The vertical dimension is defined on  $z$  coordinates. The primitive equations of fluid motion are solved with applied hydrostatic and Boussinesq approximations. In the setup presented here, the vertical turbulent viscosity and diffusivity are parameterized by a TKE mixing scheme (Gaspar et al., 1990; Gutjahr et al., 2021). Biharmonic operators are used for the velocity closure. Sea ice advection and thermodynamics are included by a coupling with the sea ice model FESIM (Danilov et al., 2015).

The biogeochemistry component of ICON-O is the Hamburg Ocean Carbon Cycle model HAMOCC (Maier-Reimer et al., 2005; Ilyina et al., 2013) in its CMIP6 version (Mauritsen et al., 2019). This version was transferred from the Earth system model MPI-ESM to ICON-O as the ocean component of the upcoming Earth system model ICON-ESM (Jungclaus et al., in prep.). Marine biology dynamics is represented by a NPZD-type approach (Six & Maier-Reimer, 1996). Sequestration of inorganic carbon and nutrients by phytoplankton growth is controlled by light availability, water temperature, and co-limitation of the macro nutrients phosphate and nitrate as well as iron, assuming Redfield stoichiometry (Six & Maier-Reimer, 1996; Kloster et al., 2006). Biogeochemical transformation processes distinguish between oxic, sub- and anoxic conditions, accounting for bacterial decomposition, denitrification, and sulfate reduction. The nitrogen cycle includes a prognostic representation of N-fixation at the sea surface by cyanobacteria (Paulsen et al., 2017). A 3-dimensional sediment module accounts for deposition and dissolution of particulate matter at the sea floor as well as benthic-pelagic pore water exchange (Heinze et al., 1999). In the current setup, tracer advection is calculated by the physical component of the model.

### 2.2 Model extensions for ICON-Coast

Starting from the model setup described in the previous section, our improvements regarding shelf-specific process representation comprise the incorporation of tidal currents including bottom drag effects, and the implementations of sediment resuspension, temperature-dependent remineralization in the water column and sediment, riverine matter fluxes from land including terrestrial organic carbon, and variable sinking speed of aggregated particulate matter. Brief introductions to these concepts and their relevance for coastal carbon dynamics are given in the results section 3.

Tidal currents are used as implemented by Logemann et al. (2021). The tide module accounts for the full luni-solar tidal potential to provide broad frequency tidal dynamics, including nonlinear interactions between partial tides. Effects of loading and self-attraction are neglected in this first version of the module.

Sediment resuspension is implemented as described in Mathis et al. (2019). Critical bed shear stresses are calculated from the mean sediment density and grainsize at every time step. The erosion depth is derived from bottom current velocities inducing overcritical bed shear stress. Here, this has been extended to account for mixing of eroded pore water with the tracer concentrations in the bottom layer of the water column, in addition to the erosion and advection of the solid sediment constituents (detritus, opal, calcium carbonate, and dust).

To incorporate a mechanistic representation of the vertical export dynamics of biogenically bound carbon and nutrients from the euphotic zone to the interior of the ocean, we adopted a scheme for marine aggregates following Maerz et al. (2020). The formulation

199 explicitly accounts for the influences of size, microstructure, heterogeneous composition,  
 200 density, and porosity of marine aggregates on their settling velocities and exposure to bio-  
 201 geochemical transformation processes. Ballasting (biogenic and lithogenic) minerals and  
 202 particulate organic carbon are tied together, yielding common but variable sinking speeds  
 203 for all aggregate components.

204 The integration of marine aggregates enables us to introduce a general temperature-  
 205 dependence for remineralization and dissolution processes of particulate matter, as the par-  
 206 ticulate components in the water column no longer sink with individual settling velocities.  
 207 Also here, we follow Maerz et al. (2020) with a Q10 approach to modify the remineralization  
 208 rate of detritus and the dissolution rate of opal, and extend this concept to dissolved organic  
 209 carbon.

210 Temperature-dependent non-linear degradation rates were also reported for the upper  
 211 sediment, derived from in-situ measurements, diagenetic modeling, and laboratory incuba-  
 212 tion experiments (Arndt et al., 2013; Franzo et al., 2019). Consistent with the Q10 approach  
 213 in the water column, we extended the temperature-dependence of the degradation of par-  
 214 ticulate organic matter and opal to the sediment. Here, we use a Q10 value of 2.3 with a  
 215 reference temperature of 10°C for detritus (Provoost et al., 2013) and a Q10 value of 2.3  
 216 with reference temperature of 20°C for opal (Kamatani, 1982; Ridgwell et al., 2002).

217 River mouths are treated as point sources at individual coastal grid cells, incorporating  
 218 the work by Lacroix et al. (2020) who investigated the influence of riverine matter fluxes on  
 219 the preindustrial oceanic CO<sub>2</sub> outgassing with the global Earth system model MPI-ESM.  
 220 Rivers are discharging prescribed fluxes of fresh water, nutrients, terrestrial organic carbon,  
 221 inorganic carbon, and alkalinity.

222 All process extensions compared to the standard configuration of HAMOCC (Mauritsen  
 223 et al., 2019) were individually evaluated during their original developments for the Earth  
 224 system model MPI-ESM and can be found in the primary references given above, including  
 225 descriptions of the mathematical formalisms.

### 226 **2.3 Regional grid refinement**

227 The other central concept of ICON-Coast, besides the incorporation of shelf-specific  
 228 processes, is the application of a regionally refined numerical grid. This is done to resolve  
 229 shelf sea dynamics more properly, while reducing resource demands compared to simulations  
 230 with a globally uniform high resolution.

231 Increasing horizontal resolution is assigned locally according to three geometric criteria  
 232 (Logemann et al., 2021): decreasing distance to the coast, decreasing water depth, and  
 233 increasing slope of the bottom topography. By combining these criteria we obtain higher  
 234 resolution in the near-coastal zones as well as the shallow shelves, broadly including the shelf  
 235 breaks as the transition to the open ocean. Areas of different resolutions are connected by  
 236 cell bisection and subsequent local spring optimization to assure smooth grid spacing and  
 237 avoid critically distorted cell geometries. An example of a grid configuration used in this  
 238 study is shown in Fig. 2.

239 The grid refinement accounts for a more detailed discretization of topographic features  
 240 in the coastal ocean, enabling a better representation of the general circulation in shelf and  
 241 marginal seas. In particular, many ocean-shelf exchange mechanisms such as cross-slope  
 242 bottom transport, instabilities of frontal boundary currents, or eddy-shelf interaction are  
 243 strongly influenced by ageostrophic processes which can be significantly better resolved by  
 244 meso-scale grid resolutions (Karakaş et al., 2006; Oguz et al., 2015; Brink, 2016; Graham  
 245 et al., 2018b; Thévenin et al., 2019; Combes et al., 2021; Kämpf, 2021). Moreover, an  
 246 increased grid resolution permits the local development of high horizontal temperature and  
 247 salinity gradients which enhances the baroclinic components of the general circulation. As all

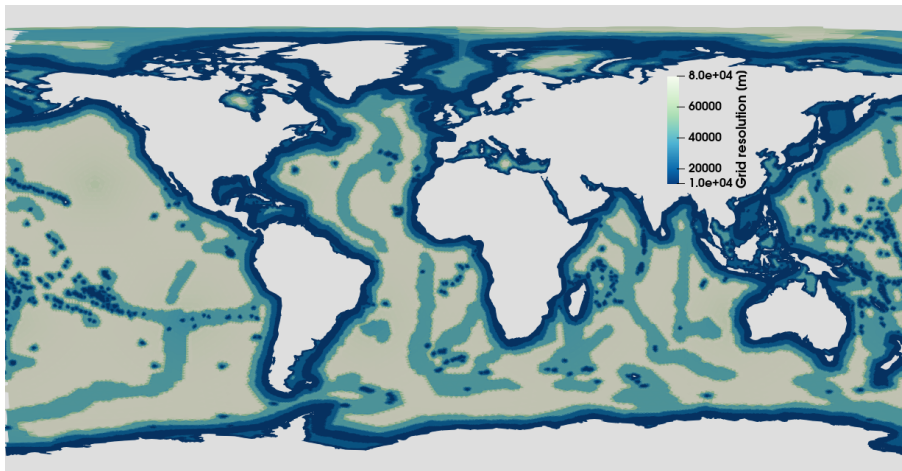


**Figure 2:** Grid configuration used for the high-res simulations with a horizontal resolution ranging from 80 km in the open ocean to 10 km at the coast lines and continental margins. For the low-res simulations, a qualitatively similar configuration has been used with a horizontal resolution that is coarser by a factor of 2, ranging from 160-20 km

248 biogeochemical tracers in the model are advected as passive tracers, the better representation  
 249 of the circulation is vital for improving the simulated biogeochemical state of the coastal  
 250 ocean.

251 Due to the applied slope criterion, a moderate refinement is also assigned to mid-ocean  
 252 ridges, seamounts, and submarine banks (Fig. 2). This accounts for a better representation  
 253 of the abyssal circulation in the open ocean, associated with tidal mixing (Simmons et al.,  
 254 2004; Dale & Inall, 2015) as well as transport of heat and biogeochemical tracers parallel to  
 255 the ridge’s flanks (Lavelle et al., 2012). Moreover, the capture of bathymetric gaps, such as  
 256 fracture zones, determines how much deep water can pass between ocean basins and where  
 257 this exchange occurs (Gille et al., 2004).

258 The spatial positioning of variables within the numerical grid follows an Arakawa C-grid  
 259 staggering, with scalar variables at the cell centre and normal components of the velocity  
 260 vector at cell boundaries. This staggering type is numerically advantageous. For triangular  
 261 cells, however, it is associated with spurious discontinuities in the divergence field of the  
 262 horizontal flow (Stuhne & Peltier, 2009; Danilov, 2010). To overcome this problem, the dis-  
 263 cretization of the primitiv equations of fluid motion is based on a novel technique developed  
 264 by Korn (2017), which provides an efficient way to control divergence noise without violating  
 265 conservation conditions. The numerical stability of strongly irregular grids as used in our  
 266 simulations was demonstrated by Logemann et al. (2021), who conducted comprehensive  
 267 test simualtions with the core model ICON-O.

## 268 2.4 Experiment design

269 In this paper, we show results from two ICON-Coast simulations with different hori-  
 270 zontal grid configurations. The first one spans a resolution of 160-20 km (low-res) and has  
 271 been run in coupled physics-biogeochemistry mode. The resolution of the second configu-  
 272 ration is higher by a factor of 2, spanning 80-10 km (high-res; Fig. 2), and has been run in  
 273 physics-only mode to assure reasonable simulation progress and computational cost. The  
 274 advantage of including the high-res simulation, albeit in a light version, is that we can bet-  
 275 ter demonstrate the benefit of a regional grid refinement for the representation of relevant  
 276 hydrodynamic features in the coastal ocean that provide the background conditions for the  
 277 biogeochemical processes. In particular at the upper end of the resolution range (10 km),

we reach or come close to the first baroclinic radius of deformation in many shelf seas and ocean-shelf transition zones, thus incorporating mesoscale activity more extensively than in the low-res simulation (Hallberg, 2013; Hewitt et al., 2017). Representing the mesoscale explicitly was shown to tangibly improve the simulated mean ocean state as well as the temporal variability (Hewitt et al., 2020). For both grid configurations, the vertical dimension is resolved by 40 layers with a surface layer thickness of 16 m, a layer thickness of 10 m in the remaining upper 100 m of the water column, and increasing thicknesses below. The high surface layer thickness is necessary in this model setup to allow for critical tidal amplitudes and sea ice formation, as a wetting-drying algorithm is not yet included. Internal model time steps are 400 s for the low-res and 100 s for the high-res setups.

The simulations were driven with ERA-Interim reanalysis data (Dee et al., 2011) of 6-hourly atmospheric forcing fields for the period 1990-2010. River runoff data are taken from a hindcast reconstruction by the global hydrological discharge model HD (Hagemann & Dümenil-Gates, 2001) for the period 1979-2009 and applied as monthly climatological means. The hindcast was generated by applying the HD model (vs. 1.10) to a simulation of the land surface scheme JSBACH (Ekici et al., 2014) forced by bias corrected ERA-Interim data (Hagemann et al., 2020). Lateral discharge fluxes were calculated globally at  $0.5^\circ$  resolution and comprise about 2000 catchments areas. Riverine inputs of DIP, DIN, DSi, DFe, DIC, Alk, tDOM (terrestrial dissolved organic matter) and POM are derived from Lacroix et al. (2020, 2021b) for about 850 rivers. In these studies, historical river loads for the period 1905-2010 were reconstructed based on a hierarchy of weathering and terrestrial organic matter export models as well as the global data set NEWS2 (Seitzinger et al., 2010). Non-weathering sources of nutrients, C and Alk from fertilizer, sewage, and allochthonous inputs were also considered.

Both simulations, low-res and high-res, were initialized by temperature and salinity fields taken from the  $0.25^\circ$  resolution World Ocean Atlas 2013 data set (Locarnini et al., 2013; Zweng et al., 2013) and an ocean at rest. Because of high computational resource demands, we so far have only performed comparatively short simulations of maximum 20 consecutive years. The biogeochemical initial state of the low-res run was therefore taken from previous test and calibration runs in order to reduce effects of long-term drift as much as possible. To apply this strategy, we could not yet account for contemporary increasing atmospheric  $p\text{CO}_2$  but used a constant preindustrial level of 278 ppm. The simulated  $\text{CO}_2$  fluxes at the sea surface are thus expected to be biased towards weaker uptake and stronger outgassing compared to observational products of the recent past. The results shown here finally stem from a repetition of the period 2000-2010, where no model parameters have been adjusted further. While being aware of associated limitations, with this approach we aim for a first-order understanding of the added value of the global coastal setup and resulting dynamics therein.

### 3 Results

#### 3.1 Global patterns of primary production and surface $\text{CO}_2$ flux

Simulated global patterns of marine net primary production and ocean-atmosphere  $\text{CO}_2$  flux are shown in Fig. 3. The general distributions of both variables reflect the persistent large-scale features and global patterns known from observational products (e.g. Takahashi et al., 2002; Holt et al., 2009; Park et al., 2010; Boyd et al., 2014; Landschützer et al., 2016; Kulk et al., 2020) and global ocean-biogeochemistry models (e.g. Laufkötter et al., 2015; Hauck et al., 2020; Séférian et al., 2020).

High biological productivity in the open ocean is linked to favorable light conditions and continuous or seasonal nutrient supply to the euphotic zone via upwelling or deep mixing. Thus, enhanced primary production is found in the equatorial Pacific, the eastern upwelling areas, and the subpolar gyres, whereas the oligotrophic subtropical gyres are

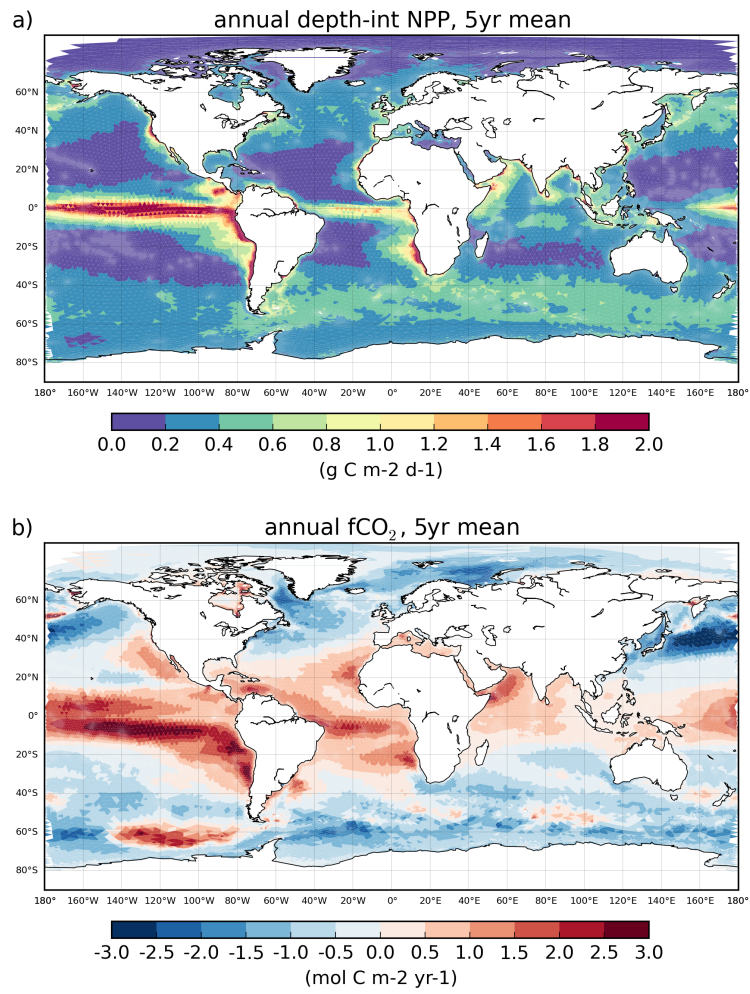


**Figure 3:** Global distributions of annual depth-integrated net primary production (a) and ocean-atmosphere CO<sub>2</sub> flux (b), simulated with low-res configuration. Positive values in (b) refer to oceanic outgassing.

328 substantially less productive throughout the year. In the Arctic Ocean, phytoplankton  
 329 growth is weak due to the sea ice cover and limited light availability. The simulated global  
 330 net primary production amounts to 49-52 Gt C yr<sup>-1</sup> (min-max during the simulation period)  
 331 with a positive drift of about 0.09 Gt C yr<sup>-1</sup> (derived from linear regression).

332 Regarding surface CO<sub>2</sub> fluxes, low latitudes are dominated by strong outgassing in  
 333 particular in upwelling areas, with maximum net fluxes in the equatorial Pacific. Middle  
 334 and high latitudes, by contrast, function as net sinks for atmospheric CO<sub>2</sub>, governed by  
 335 surface cooling and high seasonal biological export production. Deviations lie well within  
 336 the CMIP5/6 model spreads (S  ferian et al., 2020), with our model showing biases of  
 337 overestimated outgassing in low latitudes and underestimated outgassing in the Southern  
 338 Ocean. The global integral amounts to 0.1-0.2 Gt C yr<sup>-1</sup> outgassing with a negative drift  
 339 of about -0.03 Gt C yr<sup>-2</sup>. Note that the observed contemporary global uptake in the or-  
 340 der of 2 Gt C yr<sup>-1</sup> is not met because we have run ICON-Coast with constant preindustrial  
 341 pCO<sub>2</sub> in the atmosphere (section 2.4), thus approaching equilibrium conditions with net  
 342 zero surface CO<sub>2</sub> fluxes.

343 In general, the main biogeochemical features of the global open ocean are reasonably  
 344 well represented as compared to earlier model studies, such as Laufk  tter et al. (2015),  
 345 Hauck et al. (2020) and S  ferian et al. (2020). It is thus worth turning the emphasis to the  
 346 core of ICON-Coast, the coastal and shelf sea regions.

### 347 **3.2 Shelf sea dynamics**

348 The main motivation behind the development of ICON-Coast is a better representa-  
 349 tion of carbon dynamics in the coastal ocean (Fig. 1). For further evaluation, we therefore  
 350 focus on three temperate coastal regions that share the large influence of tidal currents but  
 351 differ through their embedding in the large-scale ocean circulation (Fig. 4): the Northwest  
 352 European Shelf (NWES), the Patagonian Shelf (PS), and the East China Shelf (ECS). The  
 353 NWES is connected to the eastern boundary current system of the North Atlantic subpolar  
 354 gyre (SPG). The physical and biogeochemical characteristics of water masses flushing the  
 355 shelf are strongly influenced by the strength of the SPG and the wintertime mixed layer  
 356 depth in the Northeast Atlantic (H  t  n et al., 2017; Koul et al., 2019). The PS is connected  
 357 to the Antarctic Circumpolar Circulation (ACC) passing through the Drake Passage, and  
 358 the northward flowing Malvinas Current (MC) branching off the ACC. Shelf water mass  
 359 characteristics are modulated by the inflow of Subantarctic water and shelf break upwelling  
 360 induced by the variability of the MC (Combes & Matano, 2018). The ECS is connected to  
 361 the western boundary current of the North Pacific subtropical gyre. The water masses of  
 362 this shelf sea mainly originate from the Kuroshio Current and are strongly influenced by  
 363 the strength of the Yellow Sea Warm Current branching from the Kuroshio Current during  
 364 boreal winter (Yuan et al., 2008; Lie & Cho, 2016). All three shelf regions are known to  
 365 be net sinks for atmospheric CO<sub>2</sub> under present-day climatic and environmental conditions,  
 366 driven by high biological carbon sequestration and an efficient export of respiratory CO<sub>2</sub>  
 367 to the adjacent deep ocean (e.g. Becker et al., 2021; Kahl et al., 2017; Jiao et al., 2018).  
 368 Moreover, they are subject to a strong seasonality of both the atmospheric forcing and the  
 369 response of the physical and biogeochemical conditions in the ocean, and were extensively  
 370 investigated by observational and regional modeling studies. These shelf areas thus serve as  
 371 pivotal regions to test and evaluate our new model implementations.

372 In general, we show results of biogeochemical parameters from the low-res simulation  
 373 but physical parameters from the high-res simulation (see section 2.4). This is done to  
 374 best emphasize the potentials of ICON-Coast in regional high-resolution modeling at the  
 375 global scale, as well as to demonstrate the ability of the model to simulate key processes of  
 376 marine coastal carbon dynamics. The following examples given for the three focus regions  
 377 are monthly, seasonal, or annual means over the last 5 years of our simulations, that is  
 378 2006-2010.

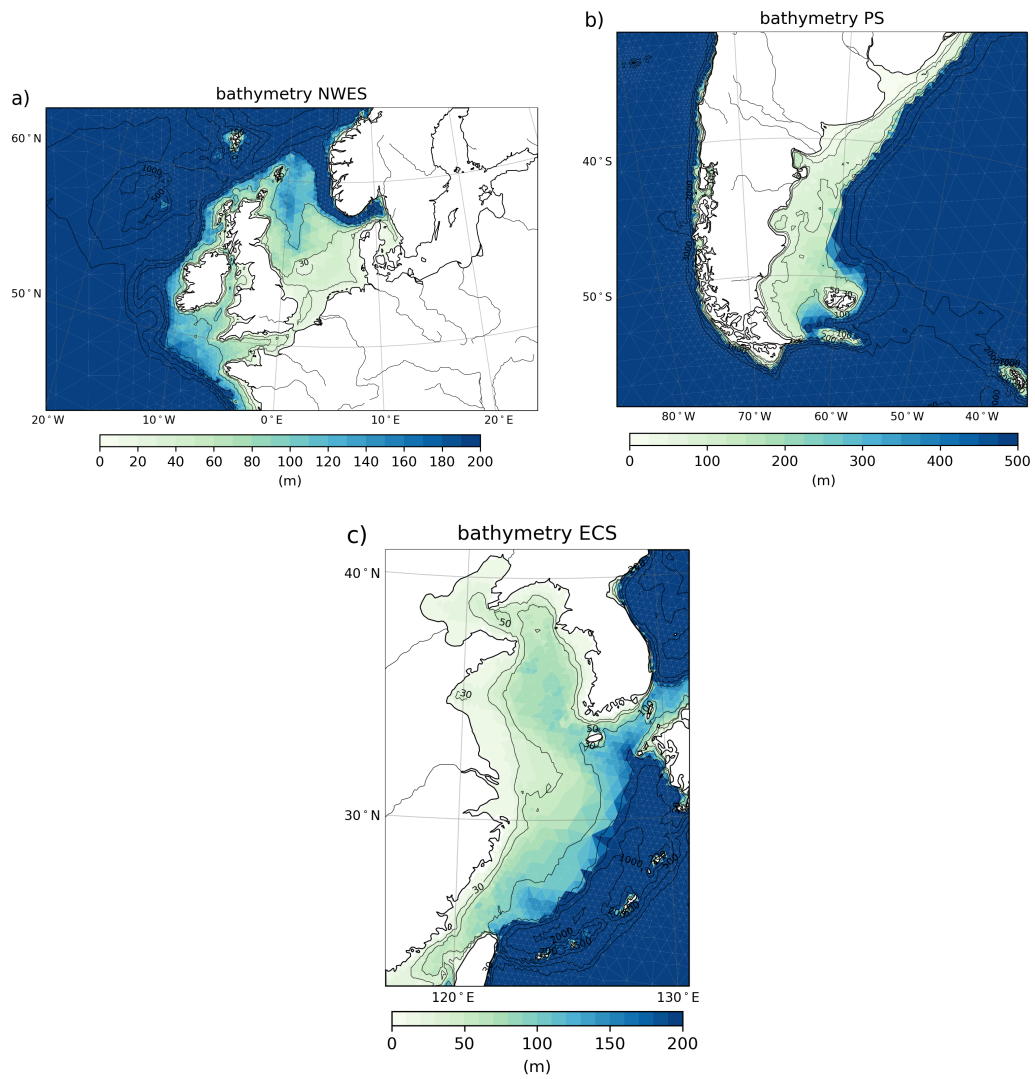


**Figure 4:** Model bathymetry of the Northwest European Shelf (a), Patagonian Shelf (b) and East China Shelf (c). Isobaths correspond to water depths of 30, 50, 100, 200, 500, 1000, 2000, and 3000 m.

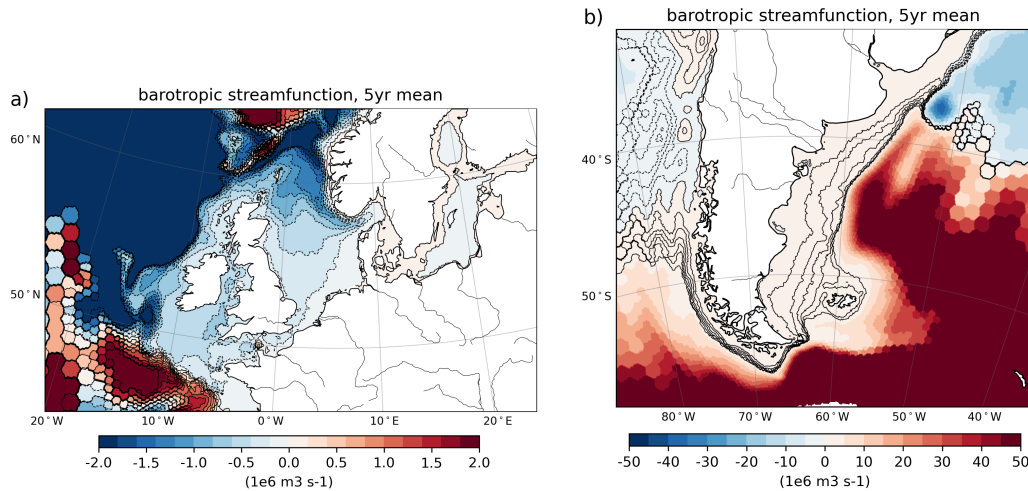


**Figure 5:** Annual mean barotropic stream function on the Northwest European Shelf (a) and Patagonian Shelf (b), simulated with high-res configuration. Increments of shown streamlines are 0.2 Sv for (a) and 0.5 Sv for (b)

### 3.2.1 General circulation

379

380

381

382

383

384

385

386

387

388

389

390

391

The general circulation of shelf seas governs the advective export of sequestered carbon from the coastal to the open ocean as well as the import of nutrient-rich water masses from deeper levels via shelf break upwelling and vertical mixing (Fig. 1 index 1; Painter et al., 2016; Legge et al., 2020; Luisetti et al., 2020). The circulation in the proximal coastal zone determines the distribution of river discharge and nutrient loadings in the inner shelf areas, as the position of river plumes is typically more sensitive to the wind direction than to the river outflow variability (Pimenta et al., 2005; Kastner et al., 2018; Kerimoglu et al., 2020). The strength and structure of the general circulation therefore sensitively influences the residence times of imported water masses on the shelves, and hence the local physical and biogeochemical water mass characteristics (Pätsch et al., 2017; X. Liu et al., 2019; Lacroix et al., 2021a). A proper representation of the general circulation is thus key for investigating coastal carbon dynamics and constraining budget uncertainties.

392

393

394

395

396

397

398

399

On the NWES, the simulated mean circulation shows all characteristic features of the well-studied North Sea circulation (Fig. 5a). The Fair-Isle Current, East-Shetland Flow, the inflow along the western side of the Norwegian Trench which recirculates in the Skagerrak and leaves the North Sea via the Norwegian Coastal Current, the Dooley Current, and the weak cyclonic circulation in the southern North Sea (Holt & Proctor, 2008; Sündermann & Pohlmann, 2011) are all well captured by ICON-Coast. The simulated net transport through the North Sea varies between 1.6-1.8 Sv and lies within the range of 0.9-2.3 Sv found in the literature (Mathis et al., 2013; Quante et al., 2016).

400

401

402

403

404

405

406

407

The circulation on the PS is more homogeneous than on the NWES (Fig. 5b). Part of the Cape Horn Current turns onto the shelf between the South American mainland and the Falkland Islands and generally flows northward to meet the La Plata river plume and the Brazil Malvinas Confluence (Combes & Matano, 2018). The inflow of the Cape Horn Current to the shelf is about 2.5 Sv simulated by ICON-Coast and has been quantified by a high-resolution regional model study to about 1.7 Sv (Guihou et al., 2020). This is a reasonable agreement, assuming similar variability and uncertainty ranges as for the well-studied NWES.

408

409

On the ECS, distinct seasonal circulation patterns are driven by the characteristic monsoon wind regimes. In winter, the Yellow Sea Warm Current branches from the Kuroshio

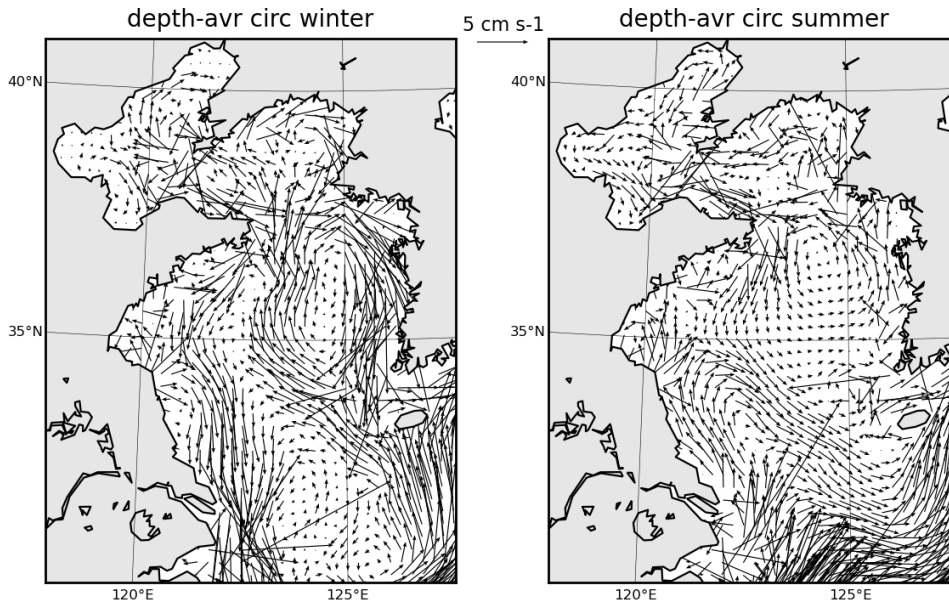


**Figure 6:** Depth-averaged current velocities on the East China Shelf for winter (left) and summer (right), simulated with high-res configuration.

410 Current and flows northward into the Bohai Sea (Wu et al., 2016). This ECS inflow is  
 411 balanced by the southward flowing Korean and Chinese coastal currents. In summer, the  
 412 whole pattern changes into a cyclonic recirculation through the entire Yellow Sea and Bohai  
 413 Sea (Zhu et al., 2015). ICON-Coast is able to capture the main features of this marked  
 414 seasonality with great detail (Fig. 6). We can even identify the anticyclonic circulation in  
 415 the northern part of the Bohai Sea in winter and its cyclonic turn in summer (Yang et al.,  
 416 2019).

### 417 *3.2.2 Tidal waves*

418 The most energetic flows in the coastal ocean are generated by tidal waves, with max-  
 419 imum current speeds exceeding 60 cm/s twice a day (Poulain & Centurioni, 2015). The  
 420 interaction with the topography in shallow areas induces energy dissipation via bottom fric-  
 421 tion and leads to high bed shear stresses and turbulent mixing in the water column (Fig. 1  
 422 index 2; Wilson & Heath, 2019). These effects are known to play an important role in the  
 423 coastal nutrient and carbon dynamics (Cadier et al., 2017; Zhao et al., 2019).

424 In our model, tidal waves are calculated from the full luni-solar tidal potential. As  
 425 shown by Logemann et al. (2021), the simulated amphidromic patterns as well as tidal  
 426 amplitudes for both the open ocean and coastal areas agree well with tidal charts derived  
 427 from gauge measurements and satellite altimetry data (e.g. Egbert & Erofeeva, 2002). Here,  
 428 we exemplify simulated M2 amplitudes for the complex tidal system of the NWES (Fig. 7)  
 429 and elaborate more on the effects of the tide-induced currents related to carbon dynamics on  
 430 the NWES, PS and ECS in the following sections. Simulated M2 amplitudes reach around  
 431 1.5 m in the German Bight area, between 1.5-2 m along the British North Sea coast and  
 432 maximum heights exceeding 3 m in the English Channel and Celtic Sea. These values as  
 433 well as the positions of the 5-6 amphidromic points on the NWES are in good agreement  
 434 with the tidal chart given e.g. by Reynaud & Dalrymple (2012).

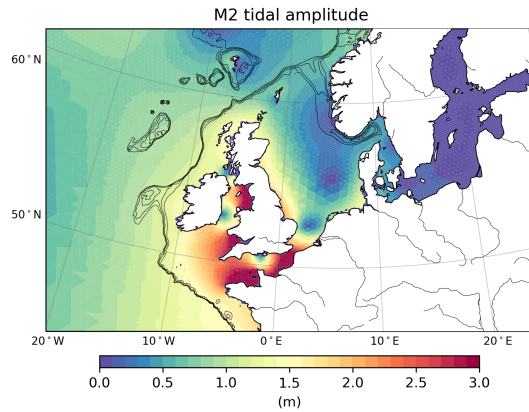


**Figure 7:** Tidal amplitudes of the semi-diurnal component M2 on the Northwest European Shelf, simulated with high-res configuration. Isobaths illustrate the shelf break at water depths of 200-500 m.

### 3.2.3 Seasonal stratification

On temperate shelves, tidal mixing is able to break the summer stratification and in many shallow areas the water column stays vertically mixed throughout the year (van Leeuwen et al., 2015). In deeper areas, the characteristic seasonal stratification prevents respiratory  $\text{CO}_2$  below the pycnocline to exchange with the atmosphere (Thomas et al., 2004; Bianchi et al., 2005; Rippeth et al., 2014). Sharp changes in ocean-atmosphere  $\Delta p\text{CO}_2$  of up to 150 ppm across tidal fronts are often observed (Bianchi et al., 2005). The strength of the stratification as well as its spatial extension and timing in the year thus are key elements of the shelf carbon pump, promoting horizontal export of sequestered carbon to the deep open ocean.

Conventional global ocean models are typically run without tides (Taylor et al., 2012; Eyring et al., 2016). Tidal waves mainly transport energy but very little mass (Toffoli & Bitner-Gregersen, 2017), and in the open ocean the local net effects of tides are negligibly small for most applications. Hence, tides are usually omitted in global simulations to save resources. As a consequence, the simulated summer stratification on temperate shelves is too strong and its spatial extension too large, covering also the shallow areas otherwise subject to strong tidal mixing (Holt et al., 2017; Mathis et al., 2018).

The strength of the seasonal stratification as simulated by ICON-Coast (Fig. 8) is in good agreement with regional high-resolution model studies (Graham et al., 2018b; Guihou et al., 2018) as well as observation-based estimates of the position of the tidal front (Bianchi et al., 2005; Yao et al., 2012; Kahl et al., 2017). The stratification might be a bit too weak on the southern PS compared to Kahl et al. (2017) but fits better with the pattern derived by Bianchi et al. (2005). Both studies analyze observational data of 5-7 year periods prior to our analysis period 2006-2010. Nevertheless, the transition from stratified to vertically mixed conditions is mainly determined by the local tidal current speed, the water depth, and the thermal forcing depending on the time of the year. The positions of tidal fronts are therefore rather stable with low interannual variability (Acha et al., 2004; Holt & Proctor, 2008).

### 3.2.4 Sediment resuspension

Another important effect of tidal currents is their contribution to the strong benthic-pelagic coupling of temperate shelves (Fig. 1 index 3). Elevated flow speeds near the bottom are known to induce critical bed shear stresses that lead to resuspension of deposited partic-

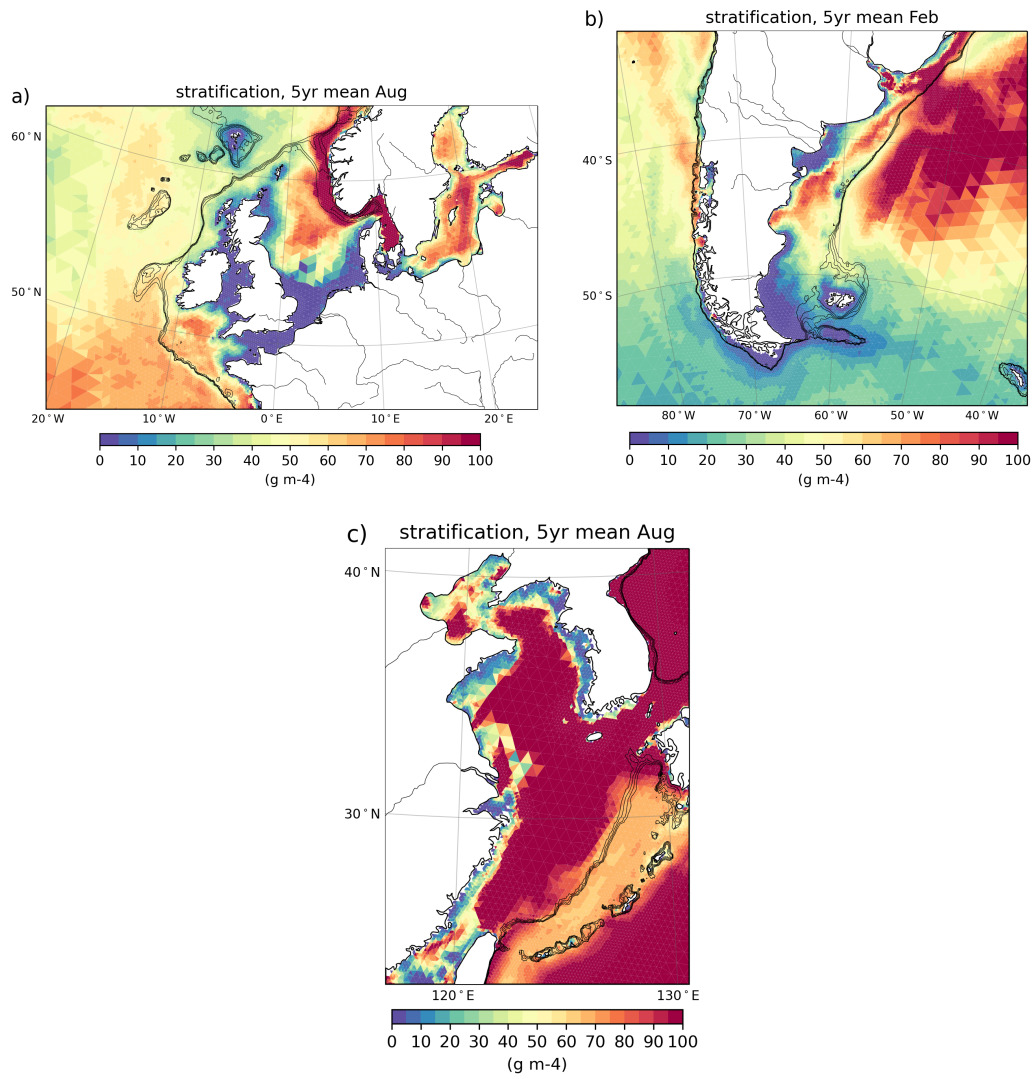


**Figure 8:** Strength of summer stratification (maximum vertical density gradient) on the Northwest European Shelf (a), Patagonian Shelf (b) and East China Shelf (c), simulated with high-res configuration. Isobaths illustrate the shelf break at water depths of 200-500 m.

467 ulate matter (Wilson & Heath, 2019). Areas with strong tidal currents thus typically have  
468 very low carbon stocks in the sediment ( $<1\%$  TOC dry weight in the upper 10 cm) and  
469 essentially net zero accumulation rates (Legge et al., 2020; T. T. Diesing M. & Bjarnadóttir,  
470 2021). As a consequence, such areas do not function as significant long-term carbon storage.  
471 The resuspension of settled organic material and nutrient-rich pore water from sediments  
472 back to the water column, though, delivers nutrients for pelagic organisms (F. Liu et al.,  
473 2014). This mechanism contributes to the high biological productivity and  $\text{CO}_2$  uptake in  
474 tidally mixed areas of temperate shelves in summer. The enhanced turbidity due to resus-  
475 pended particulate matter, however, also reduces irradiance and thus can negatively affect  
476 phytoplankton growth (Loebl et al., 2009; Su et al., 2015; Zhao et al., 2019).

477 In ICON-Coast, we have implemented a sediment resuspension scheme following Mathis  
478 et al. (2019). Critical bed shear stresses and the fraction of deposited material that is eroded  
479 are inferred from the near-bottom flow speed and the density and grain size of the mean  
480 sediment composition. This dynamical approach enables the simulation of the seasonal  
481 cycle of sediment stability and wind-induced resuspension. For our developments, we have  
482 initialized the sediment from a historical simulation of the global Earth system model MPI-  
483 ESM (Mauritsen et al., 2019). This model, however, did not account for resuspension  
484 processes and therefore has a uniform distribution of highly overloaded carbon contents in  
485 coastal sediments, exceeding 20% TOC dry weight (not shown).

486 During the first 2-3 decades simulated by ICON-Coast, much of the deposited carbon  
487 gets eroded from the sediment and remineralized in the water column (Fig. 9). The patterns  
488 of low carbon content ( $<1\%$  TOC dry weight) on the NWES generally agree well with  
489 measured distributions shown in Legge et al. (2020) and tide-induced high bed shear stresses  
490 reported by Wilson & Heath (2019). On the PS, the simulated carbon content reflects the  
491 observed sediment composition given in Violante et al. (2014). Over large PS areas, the  
492 sediment is dominated by sands and gravels, associated with low carbon concentrations  
493 (M. Diesing et al., 2017). Muddy sediments with high carbon concentrations are found  
494 along the shelf break and in the coastal bays between  $39\text{--}48^\circ\text{S}$ . Similarly in ICON-Coast,  
495 the shelf break as well as the coastal bays on the PS are less affected by resuspension and  
496 hence keep elevated carbon fractions in the sediment. Maximum simulated concentrations  
497 in these accumulation areas reach up to  $220\text{ kg C m}^{-3}$  in the uppermost sediment layers.  
498 Hu et al. (2011) and Yang et al. (2014) provide identifications of mud deposition centers  
499 on the ECS based on sediment core sampling. As indicated in Fig. 9c, ICON-Coast is able  
500 to capture the large deposition area in the center of the Yellow Sea as well as the higher  
501 carbon contents in the Bohai Sea.

502 In deeper shelf areas, bed shear stresses are generally weaker and critical values are  
503 rather caused by wind events (e.g. Wilson & Heath, 2019). Accordingly, net erosion rates  
504 are lower and the adjustment of the simulated sediment state takes more time. This is  
505 reflected by a longer drift in the carbon content for instance in the north-eastern part of the  
506 North Sea (Fig. 9a) and the outer shelf areas of the ECS (Fig. 9c). In these regions, relative  
507 organic carbon concentrations are still a factor of about 5 higher than in observations.

### 508 *3.2.5 Sinking of marine aggregates*

509 As another process extension of ICON-Coast, we have included an aggregate sinking  
510 scheme for particulate matter in the water column, following Maerz et al. (2020). Sinking  
511 organic and inorganic particles in the ocean tend to stick together by physical aggregation  
512 and form particulate assemblages known as marine aggregates. The variable buoyancy of  
513 marine aggregates, determined by their size and density, is associated with variable set-  
514 tling velocities that affect the vertical export of sequestered carbon out of the biologically  
515 productive euphotic zone (Fig. 1 index 4; Francois et al., 2002). This mechanism crucially  
516 contributes to the drawdown of atmospheric  $\text{CO}_2$ , as any resulting imbalance in sea wa-

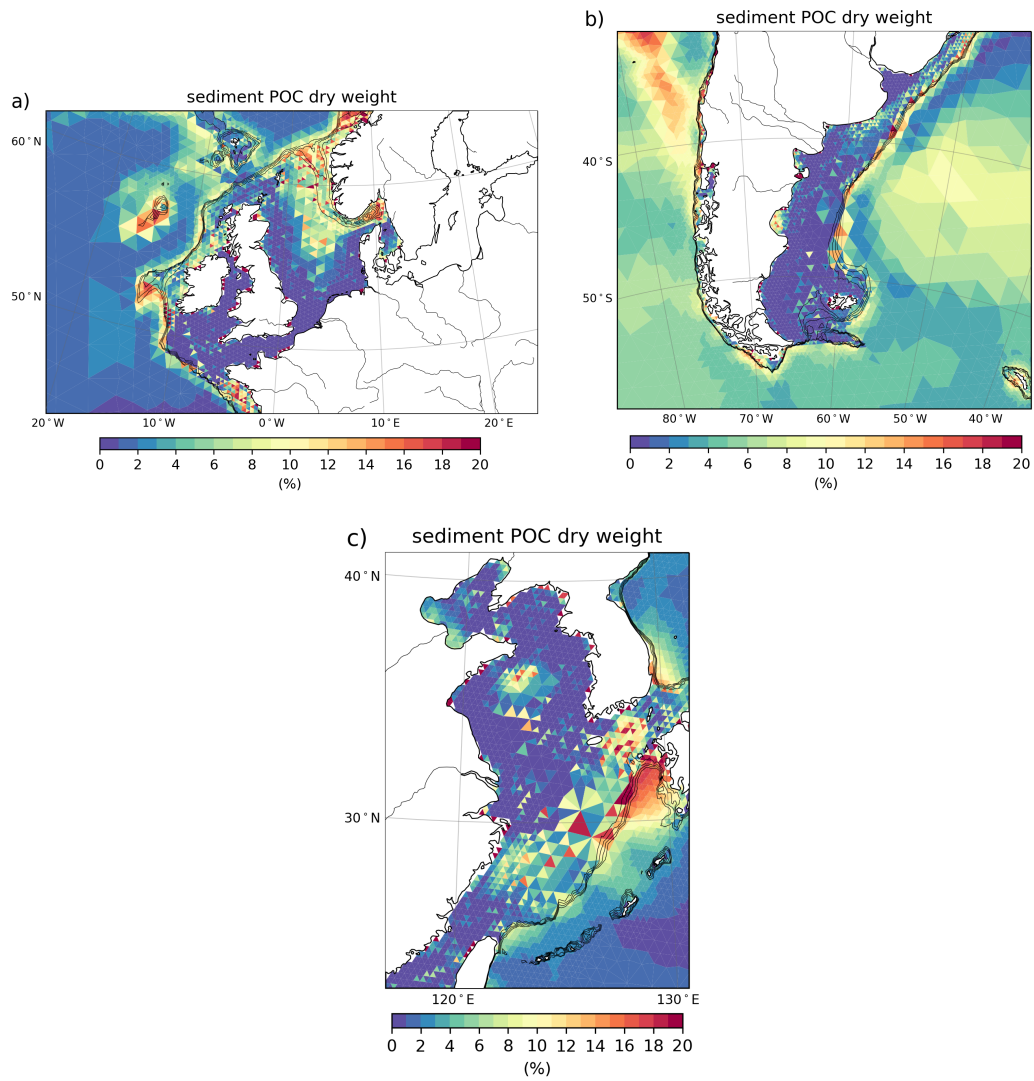


**Figure 9:** Dry weight of organic carbon in the upper 10 cm of the sediment on the Northwest European Shelf (a), Patagonian Shelf (b) and East China Shelf (c), simulated with low-res configuration. Isobaths illustrate the shelf break at water depths of 200-500 m.

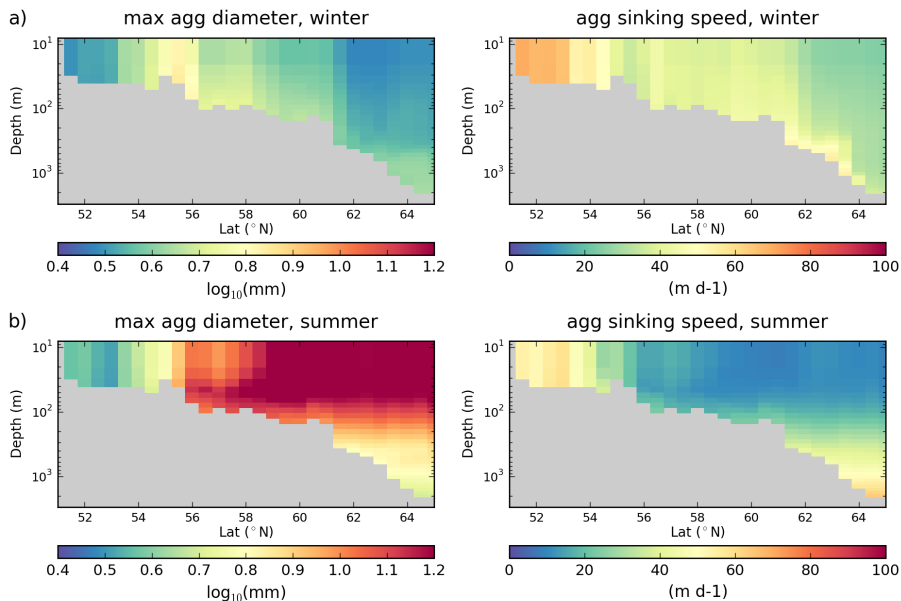


**Figure 10:** Maximum diameter (left) and mean sinking speed (right) of marine aggregates in winter (a) and summer (b) along a meridional transect through the North Sea at 2.5°E, simulated with low-res configuration.

517 ter pCO<sub>2</sub> near the ocean surface induces CO<sub>2</sub> gas exchange with the atmosphere (Volk &  
 518 Hoffert, 1985; Kwon et al., 2009).

519 Global models usually parameterize the attenuation of vertical POC fluxes through an  
 520 empirical fit to observations (Gloege et al., 2017). Power law parameterizations or expo-  
 521 nential decay rates are most widely used. Such approaches, however, lack a mechanistic  
 522 understanding and are aligned to present-day relations between primary production and  
 523 remineralization processes.

524 The sinking scheme of ICON-Coast explicitly represents the main structural and com-  
 525 positional characteristics of marine aggregates, and ties ballasting mineral and POC fluxes  
 526 together. In this way, the model is able to capture main seasonal characteristics of marine  
 527 aggregates in middle and high latitudes (Fig. 10; Fettweis et al., 2014; Maerz et al., 2016;  
 528 Schartau et al., 2019). In winter, marine primary production is weak and thus little organic  
 529 carbon is available to assemble large aggregates. The composition, therefore, is dominated  
 530 by high-density mineral components, leading to comparatively small aggregate sizes and  
 531 high sinking speeds (Fig. 10a). During summer, high productivity delivers organic carbon  
 532 to form biogenic aggregates of larger sizes but lower excess densities, and thus reduced  
 533 sinking speeds (Fig. 10b). In the open ocean and stratified shelf areas, the carbon content  
 534 gets remineralized while the aggregates sink to deeper levels, and accordingly the aggregates  
 535 decompose, become more compacted and achieve higher settling velocities. In tidally mixed  
 536 areas, by contrast, sediment resuspension prevents mineral components such as plankton  
 537 shells and terrestrial dust to become deposited (Babin & Stramski, 2004; Vantrepotte et  
 538 al., 2012). The aggregates therefore accommodate larger fractions of mineral components,  
 539 keeping sizes smaller and sinking speeds higher throughout the year.

540 Water temperature has a non-linear influence on the degradation processes of dissolved  
 541 and particulate organic carbon (Yvon-Durocher et al., 2012; Laufkötter et al., 2017; Lønborg  
 542 et al., 2018) as well as diatom silica frustules (Hurd, 1972; Dixit et al., 2001; van Cappellen  
 543 et al., 2002). In addition to the speed at which marine aggregates settle, the temperature  
 544 dependence of the compound's degradation rates is also a critical parameter since it de-

termines the sensitivity of aggregates to extensive biogeochemical transformations (Fig. 1 index 5). The strong temperature gradients in the upper ocean across latitudes and seasons thus promote spatially and temporally heterogeneous recycling rates and export fluxes, with maximum ranges being observed in the shallow coastal areas (Guidi et al., 2015; Xie et al., 2019). To account for regionally and seasonally varying degradation rates in ICON-Coast, we have implemented temperature dependencies following a Q10 approach and have extended the concept by Maerz et al. (2020) from the water column into the sediment. It is worth mentioning that all simulated seasonal aspects of aggregate composition, size and sinking speed emerge from the internal model formulation without prescribing any element of seasonality.

Another factor controlling the turnover rates of organic carbon in the coastal ocean is the age of organic material settled to the sediment. Fresh, dead material in sediments of shallow areas is generally more attractive as source of carbon and energy for benthic organisms than older, more refractory material typically found in deeper areas (Arndt et al., 2013; O'Meara et al., 2018). The heterotrophic recycling of carbon and nutrients is thus accelerated in sediments of shallow areas, potentially stimulating high biological productivity by the resupply of nutrients to otherwise depleted surface waters. As our model does not incorporate metabolic reworking of organic matter by benthic communities, we approximate this age effect by a modification of the remineralization rate constant of detritus deposited at water depths of up to 500 m, assigning linearly decreasing values with increasing depth from 0.06 to 0.013 d<sup>-1</sup> at a reference temperature of 10°C.

### 3.2.6 River inputs

The importance of riverine carbon, alkalinity, and nutrient inputs for addressing regional carbon dynamics at the global scale was recently highlighted by Hauck et al. (2020) and Lacroix et al. (2020, 2021b). In conventional global biogeochemistry models, net particulate export fluxes to the sediment would violate the conservation of global budgets and induce long-term inventory drift as well as artificial gas exchange with the atmosphere. Burial losses are therefore typically balanced by instantaneous remineralization and diffusive resupply to the water column (Najjar et al., 2007) or by prescribed uniform weathering fluxes at the sea surface (Ilyina et al., 2013). In ICON-Coast, weathering fluxes and anthropogenic nutrient loadings are provided by spatially explicit river inputs (Fig. 1 index 6). This approach accounts for the influences of matter fluxes from land on the coastal carbon dynamics and allows to integrate regional, inter-compartmental fluxes as well as imbalances in global inventories under different environmental conditions and human activities (Tamburini & Föllmi, 2009; Wallmann, 2010; Beusen et al., 2016).

In our simulations we have used river loads for 1980-2010 conditions derived by Lacroix et al. (2020, 2021b) from weathering rates and terrestrial organic matter export on land, including downstream transformation processes in the catchment areas. Global integrals are compared with contemporary estimates in Table 1. One of the riverine substances released to the ocean is terrestrial dissolved organic matter (tDOM), a biogeochemical tracer usually not considered by global models to date (Lacroix et al., 2021b). tDOM is more refractory than oceanic organic matter and has a carbon-to-nutrient ratio that is about 20 times higher (Compton et al., 2000; Aarnos et al., 2018). Rivers are responsible for the largest export of tDOM to the ocean with an annual flux of about 0.2 Pg C yr<sup>-1</sup> (Bauer et al., 2013; Kandasamy & Nath, 2016), thus significantly increasing the pCO<sub>2</sub> of the coastal ocean (Lacroix et al., 2020). In our simulations, about 50% of the global terrestrial carbon input is decomposed in the coastal ocean (water depth < 200 m), lying well within the estimated range of 35-55% given in the literature (Fichot & Benner, 2014; Kaiser et al., 2017; Aarnos et al., 2018). In the broad shelf seas considered here, decomposition proportions are higher due to longer residence times of near-coastal waters (Lacroix et al., 2021a), with simulated values of 58% (of 2.1 Pg C yr<sup>-1</sup>) on the NWES, 67% (of 0.8 Pg C yr<sup>-1</sup>) on the PS, and 85% (of 6.4 Pg C yr<sup>-1</sup>) on the ECS. Other riverine substances directly affecting the surface CO<sub>2</sub>

**Table 1:** River inputs for the period 1981-2010 used in the presented ICON-Coast simulations as derived by Lacroix et al. (2020, 2021b), and contemporary observation- and model-based estimates from literature.

Compounds	ICON-Coast	Contemporary estimates	References
DIP [Tg P yr <sup>-1</sup> ]	1.2	0.8-1.4	Meybeck (1982); Compton et al. (2000); Seitzinger et al. (2010)
DIN [Tg N yr <sup>-1</sup> ]	17.6	12-19	Meybeck (1982); Seitzinger et al. (2010)
DSi [Tg Si yr <sup>-1</sup> ]	328	170-490	Beusen et al. (2009); Dürr et al. (2011); Tréguer & De La Rocha (2013); Tréguer et al. (2021)
DIC/Alk [Tg C of HCO <sub>3</sub> <sup>-</sup> yr <sup>-1</sup> ]	370	260-550	Berner et al. (1983); Amiotte Suchet & Probst (1995); Hartmann et al. (2009); M. Li et al. (2017)
DOM [Tg C yr <sup>-1</sup> ]	216	130-240	Meybeck & Vörösmarty (1999); Seitzinger et al. (2010); M. Li et al. (2019)
POM [Tg C yr <sup>-1</sup> ]	115	100-230	Meybeck & Vörösmarty (1999); Seitzinger et al. (2010); Galy et al. (2015)

597 flux are the loadings of alkalinity and dissolved inorganic carbon. As these rarely deviate  
598 from each other by more than 10% (Araujo et al., 2014; Middelburg et al., 2020), we use  
599 a mole ratio of 1:1 following Lacroix et al. (2020), which leads to a further increase in  
600 near-coastal pCO<sub>2</sub>.

### 601 3.2.7 Primary production

602 A characteristic feature of many shelf seas is their exceptionally high biological produc-  
603 tivity, which is one of the most essential drivers to lower pCO<sub>2</sub> in coastal surface waters of  
604 middle latitudes and foster CO<sub>2</sub> ingassing (Muller-Karger et al., 2005; Gattuso et al., 1998).  
605 Key processes mediating enhanced phytoplankton growth are: import of nutrient-rich water  
606 masses from the adjacent open ocean, additional continuous nutrient supply via river loads,  
607 fast internal nutrient recycling, and often strong tidal mixing, which prevents deposition of  
608 biologically bound nutrients in the sediment (Dai et al., 2013; Cao et al., 2020). In addi-  
609 tion to river loads from land, we prescribe atmospheric dust (Fe) and nitrogen deposition  
610 following Mauritsen et al. (2019), which provides another source of inorganic nutrients for  
611 marine primary production.

612 The simulated annual net primary production on the NWES (Fig. 11a) well captures  
613 the high phytoplankton growth rates in the near-coastal zones around the British Islands  
614 and along the continental coast of the southern North Sea, as well as the strong gradients to  
615 the open shelf areas of the central and northern North Sea (Moll, 1998; Provoost et al., 2010;

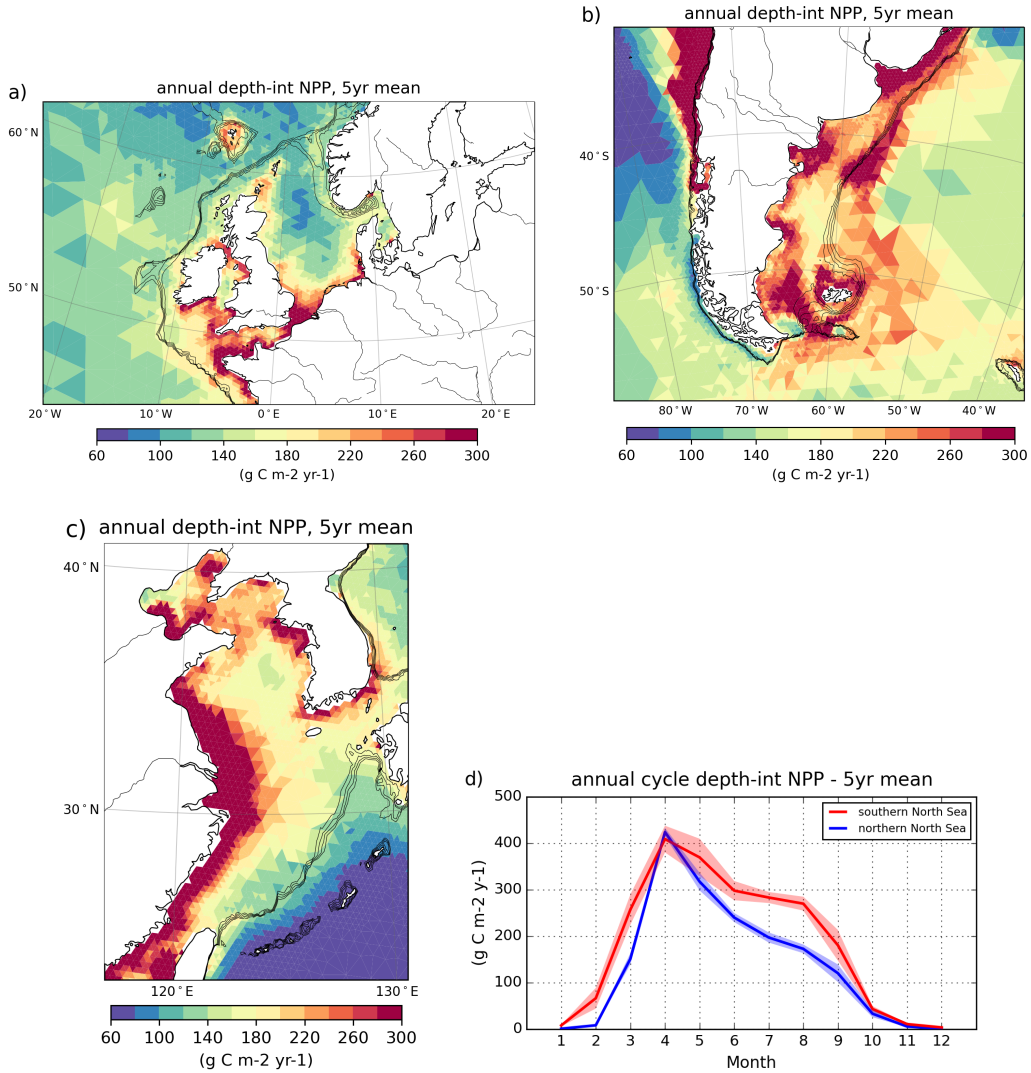


**Figure 11:** Annual depth-integrated net primary production on the Northwest European Shelf (a), Patagonian Shelf (b) and East China Shelf (c), as well as seasonal cycle in the northern and southern North Sea (d), simulated with low-res configuration. Isobaths illustrate the shelf break at water depths of 200-500 m.

616 Holt et al., 2012, 2016; Williams et al., 2013). Similarly, the seasonal cycle averaged over  
 617 the southern and northern North Sea (Fig. 11d), separated by the 50 m isobath, well reflects  
 618 the spring bloom and summer growth seasons (compare to Moll, 1998; Lemmen, 2018).  
 619 Simulated annual primary production of the entire North Sea is about  $160 \text{ g C m}^{-2} \text{ yr}^{-1}$ ,  
 620 which compares well to the range of  $100\text{-}180 \text{ g C m}^{-2} \text{ yr}^{-1}$  given in the cited observational  
 621 and regional model studies.

622 The PS is another highly productive shelf sea with an annual net primary production  
 623 of about  $350 \text{ g C m}^{-2} \text{ yr}^{-1}$  (Gonçalves-Araujo et al., 2016; Piola et al., 2018). A comparably  
 624 high phytoplankton growth is simulated by ICON-Coast (Fig. 11b). In observations, a  
 625 persistent local maximum of Chl-a concentrations is found along the northern part of the  
 626 PS shelf break, caused by shelf break upwelling of the northward flowing Malvinas Current  
 627 (Carreto et al., 2016; Franco et al., 2017). In the low-res simulations, elements of enhanced  
 628 primary production along the shelf break are also indicated, in spite of slope currents and  
 629 upwelling transports being underestimated due to unresolved meso-scale processes.

630 On the ECS, the productivity in the near-coastal zone is strongly influenced by riverine  
 631 nutrient loads, similar to the NWES (Fig. 11c). In observational products as well as in our  
 632 simulations, local maxima in net primary production of up to  $700 \text{ g C m}^{-2} \text{ yr}^{-1}$  are found in  
 633 the river plumes of the Yangtze and Yellow Rivers, discharging at the Chinese coasts of the  
 634 Yellow Sea and Bohai Sea, respectively (Tan & Shi, 2006). Also the seasonal cycle with two  
 635 pronounced phytoplankton blooms in spring and late summer is captured by ICON-Coast  
 636 (not shown), with a spring bloom though underestimated by about 20% compared to G. Li  
 637 et al. (2004); Tan & Shi (2012) and Luo (2014).

### 638 **3.2.8 Surface CO<sub>2</sub> flux**

639 In temperate shelf seas, the high biological productivity and export of dissolved inor-  
 640 ganic carbon is typically associated with a net heterotrophic state and CO<sub>2</sub> uptake from the  
 641 atmosphere (Fig. 1 index 7; Kühn et al., 2010; Becker et al., 2021; Tseng et al., 2011). In  
 642 the near-coastal zone, river loads play an important role for the air-sea gas exchange at the  
 643 global scale, as a substantial amount of the CO<sub>2</sub> uptake is caused by biological consumption  
 644 of riverine inorganic nutrients and the resulting alkalinity production (Hauck et al., 2020;  
 645 Lacroix et al., 2020). Moreover, the mixing of high-pCO<sub>2</sub> river runoff with low-pCO<sub>2</sub> sea  
 646 water has been found to induce strong CO<sub>2</sub> uptake in brackish waters of several large river  
 647 plumes across latitudes, such as the Yangtze and Mississippi plumes (Tseng et al., 2011;  
 648 Huang et al., 2015; Kealoha et al., 2020). In most high- and low-latitude coastal regions,  
 649 the temperature effect on the CO<sub>2</sub> solubility of sea water exceeds the biological CO<sub>2</sub> draw-  
 650 down, leading to net CO<sub>2</sub> outgassing in low latitudes (G. G. Laruelle et al., 2010; Mayer et  
 651 al., 2018) and net uptake in high latitudes (Arrigo et al., 2008; Yasunaka et al., 2016, 2018).  
 652 In Antarctic coastal areas, though, the net uptake might be weak, since upwelling events in  
 653 winter bring high pCO<sub>2</sub> waters to the surface and almost balance the temperature effect as  
 654 well as the biologically driven uptake in summer (Monteiro et al., 2020a, 2020b).

655 Simulated surface CO<sub>2</sub> fluxes (fCO<sub>2</sub>) are shown in Fig. 12. Because of the mixture  
 656 of driving the model with a modern climate but preindustrial pCO<sub>2</sub> (see section 2.4), the  
 657 resulting fCO<sub>2</sub> are not fully comparable with present-day observations. In our experiments  
 658 though, the spatial structures of fCO<sub>2</sub> in the coastal ocean are relatively insensitive to  
 659 variations in atmospheric pCO<sub>2</sub> ranging from preindustrial to present-day levels. We there-  
 660 fore focus more on the qualitative fCO<sub>2</sub> distributions and gradients here and reflect on the  
 661 magnitudes of the fluxes in the discussion section 4.

662 The northern North Sea and outer shelf areas of the NWES are known to be net sinks for  
 663 atmospheric CO<sub>2</sub> under present-day climatic conditions, while the shallow southern North  
 664 Sea is close to neutral (Thomas et al., 2004; Marrec et al., 2015; Kitidis et al., 2019; Becker  
 665 et al., 2021). This structure is qualitatively reproduced in our ICON-Coast simulations  
 666 (Fig. 12a) with an annual mean uptake in the North Sea of about  $0.8 \text{ mol C m}^{-2} \text{ yr}^{-1}$ .

667 The PS is a significant net carbon sink likewise (Kahl et al., 2017). Tidally mixed  
 668 coastal areas, however, are dominated by CO<sub>2</sub> outgassing in austral summer (Bianchi et al.,  
 669 2005). This seasonal feature is also captured by ICON-Coast (Fig. 12b). In the northern  
 670 part of the PS, though, the outgassing signal is overestimated and extends into the stratified  
 671 area of the open shelf.

672 The ECS is simulated as an efficient shelf carbon pump (Fig. 12c). The East China  
 673 Sea acts as a strong carbon uptake area and the Yellow Sea and Bohai Sea as rather weak  
 674 ones, which is consistent with observations (Tseng et al., 2011; Jiao et al., 2018; Song et al.,  
 675 2018). Moreover, the seasonal cycle of fCO<sub>2</sub> in the East China Sea measured by Tseng et al.  
 676 (2011) is well captured by ICON-Coast (Fig. 12d), with an uptake of about  $3 \text{ mol C m}^{-2} \text{ yr}^{-1}$   
 677 in winter and a weak outgassing of  $0.5 \text{ mol C m}^{-2} \text{ yr}^{-1}$  in summer, averaged over the same  
 678 region investigated in that study.

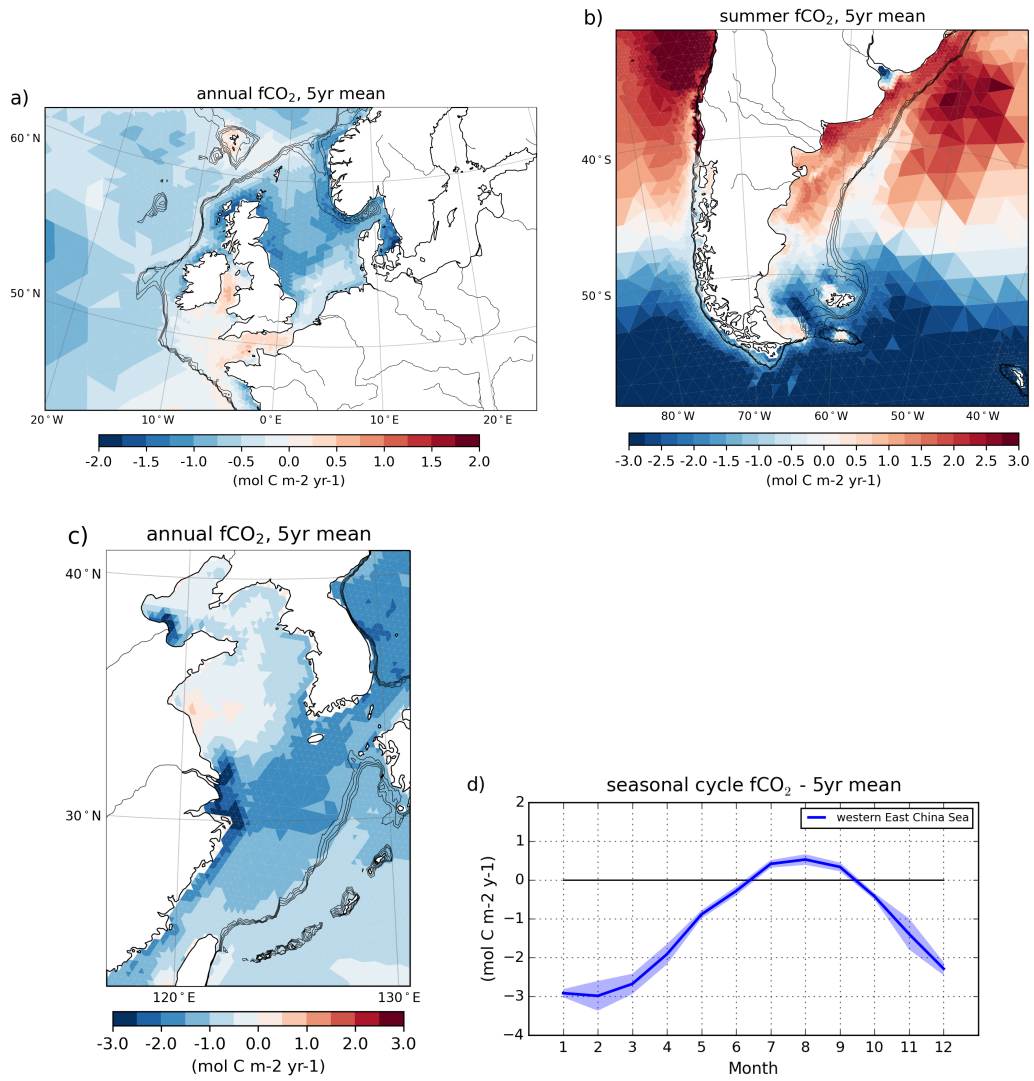


**Figure 12:** Ocean-atmosphere CO<sub>2</sub> flux for (a) the Northwest European Shelf (annual), (b) Patagonian Shelf (summer), and (c) East China Shelf (annual), as well as (d) seasonal cycle in the western East China Sea, simulated by the low-res configuration. Positive values refer to oceanic outgassing. Isobaths illustrate the shelf break at water depths of 200-500 m.

679 The CO<sub>2</sub> flux at the sea surface is a sensitive metric of the coastal carbon dynamics,  
 680 as it is affected directly or indirectly by all physical and biogeochemical processes discussed  
 681 in this section. To provide an outlook of the model skills also in coastal areas other than  
 682 the temperate shelves, we briefly elaborate on the simulated fCO<sub>2</sub> for the Sunda Shelf (as  
 683 an example of a large low latitude shelf) and the coastal ocean of the Arctic (as an example  
 684 of a high latitude region).

685 In our simulations, the whole Sunda Shelf is releasing CO<sub>2</sub> to the atmosphere on annual  
 686 means, consistent with observations and regional model studies (Kartadikaria et al., 2015;  
 687 Mayer et al., 2018; Zhou et al., 2021). The winter and summer monsoon winds drive distinct  
 688 seasonal circulation regimes on the shelf and lead to a reversed fCO<sub>2</sub> in the northern part  
 689 in winter (Mayer et al., 2018). ICON-Coast captures this seasonality with an uptake of  
 690 up to 1 mol C m<sup>-2</sup> yr<sup>-1</sup> near the Gulf of Thailand in winter and an outgassing of up to  
 691 0.8 mol C m<sup>-2</sup> yr<sup>-1</sup> in summer, while the southern shelf areas show continuous outgassing  
 692 of 0.3-0.7 mol C m<sup>-2</sup> yr<sup>-1</sup> throughout the year.

693 The Arctic ocean accomodates the world's largest continental shelves, extending up to  
 694 1500 km from the coast of Siberia into the ocean. Most of these areas draw down atmospheric  
 695 CO<sub>2</sub> via biologically mediated pCO<sub>2</sub> reduction during phytoplankton blooms and cooling of  
 696 warm water masses intruding from the North Atlantic and Pacific (Bates & Mathis, 2009).  
 697 Strong net uptake fluxes exceeding 2 mol C m<sup>-2</sup> yr<sup>-1</sup> are simulated by ICON-Coast in the  
 698 Barents Sea and the deep water formation sites of the GIN Sea, in agreement with multi-  
 699 year observations by Yasunaka et al. (2016, 2018). Regionally enhanced uptake of more  
 700 than 1 mol C m<sup>-2</sup> yr<sup>-1</sup> is also indicated in the Chukchi Sea, both in our simulations and  
 701 field measurements e.g. by Bates (2006) and Cai et al. (2010).

702 Overall, the spatial patterns of seasonal and annual fCO<sub>2</sub> simulated by ICON-Coast for  
 703 various regions agree well with observational products. In particular the skill in capturing  
 704 seasonality is a remarkable improvement, contrasting the large model-data mismatch on the  
 705 seasonal time scale of conventional global biogeochemistry models until now (Hauck et al.,  
 706 2020). Nevertheless, the net uptake fluxes in middle and high latitudes are systematically  
 707 underestimated, which can be attributed to the lower atmospheric pCO<sub>2</sub> of preindustrial  
 708 levels used in our simulations. Estimates of the change in CO<sub>2</sub> flux due to the pCO<sub>2</sub> rise  
 709 during the 20th century, derived from recent global simulations by Lacroix et al. (2021b),  
 710 show a clear latitudinal structure, with higher increases in CO<sub>2</sub> fluxes to the ocean at higher  
 711 latitudes. We therefore are optimistic that the magnitudes of the net fluxes simulated by  
 712 ICON-Coast will get closer to observations of the recent past when we increase atmospheric  
 713 CO<sub>2</sub> concentrations to present-day values. We further expect the regional and seasonal  
 714 fCO<sub>2</sub> biases e.g. on the PS to get smaller, since they are consistently resulting from too high  
 715 pCO<sub>2</sub> in the ocean relative to the atmosphere.

## 716 4 Discussion

717 We have evaluated a new global modeling approach aiming to reduce uncertainties in  
 718 the marine carbon cycle via increased grid resolution in the land-ocean transition zone and  
 719 enhanced process representation of physical and biogeochemical shelf sea dynamics. The  
 720 evaluation therefore focused on the coastal ocean, whereas in the open ocean we expect the  
 721 global patterns shown in Fig. 3, as well as their spatial integrals, to be still significantly  
 722 influenced by the initial conditions because of the comparatively short simulation periods of  
 723 10-20 years. In particular the state of the deep ocean, including the sediment composition,  
 724 is subject to long-term model drift (Heinze et al., 1999; Palastanga et al., 2011). In many  
 725 coastal regions, however, the ocean circulation and tracer distribution are rather dominated  
 726 by short-term regional-scale and even local-scale processes such as tidal mixing, river loads,  
 727 and the regional atmospheric forcing. In our test simulations, accordingly, most variables  
 728 on the shelves show a quick response to the external forcing already in the first few years,  
 729 without a strong discernable drift but a high sensitivity to changes in model-specific pa-

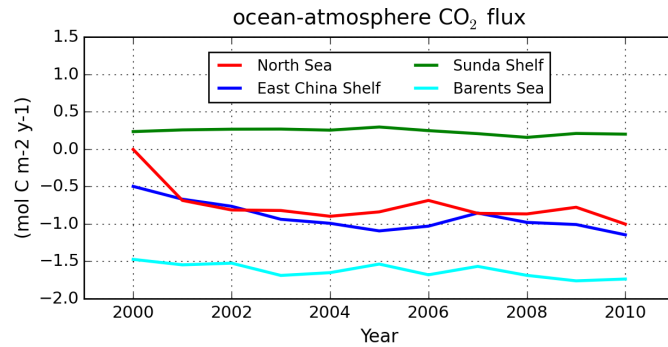


**Figure 13:** Time series of annual ocean-atmosphere CO<sub>2</sub> flux in various shelf seas, simulated by the low-res configuration. Positive values refer to oceanic outgassing.

rameters (Fig. 13). In particular the spatial patterns and gradients are rapidly developing. This characteristic allows us to gain a basic understanding about the performance of the model in various shelf and marginal seas, although the currently available model runs are relatively short.

As known from regional model studies, an increased horizontal resolution in the coastal areas generally improves the spatial manifestation of the implemented physical and biogeochemical processes (e.g. Mathis et al., 2015; Graham et al., 2018a, 2018b; Guihou et al., 2018; de Souza et al., 2020). Moreover, the structure and strength of the general circulation, including ocean-shelf exchange, gets more realistic, which affects the distribution of water masses and associated residence times (Pätsch et al., 2017; X. Liu et al., 2019; Lacroix et al., 2021a). The transport rates of boundary and slope currents, for instance, are underestimated in our low-res runs but become more energetic in the high-res simulations (not shown). The representations of the bottom topography and the orography of coastlines are further improved by the unstructured triangular grid due to the smoother horizontal discretization of topographic features compared to the typical staircase approximation by rectilinear grids. We expect, in particular, the influence of cross-shelf break transport on the coastal carbon cycle to improve further when we include the biogeochemistry model component also in the high-res simulations. In the open ocean, our physical simulations show that the increase in resolution from 160 km (low-res) to 80 km (high-res) leads to a better representation of the large-scale gyre system, reduced biases in winter mixed layer depths, and more realistic locations of the deep water formation sites (not shown). These changes reflect the general behavior of global Earth system models to increased resolution (Hewitt et al., 2020). The improved circulation should then also affect the global distribution of biogeochemical tracers such as nutrients, dissolved carbon, and alkalinity.

The concept of using unstructured variable-resolution meshes to enhance the quality of a simulation in the region of interest was developed about 1-2 decades ago (e.g. Chen et al., 2003; Pain et al., 2005; Piggott et al., 2008; Behrens & Bader, 2009) and has seen substantial progress in recent years concerning optimization, stability, and complexity (Weller et al., 2016; Remacle & Lambrechts, 2018). Applications of global grid configurations with regional refinement in the coastal ocean, however, were focused on physical ocean modeling so far (D. V. Sein et al., 2017; Hoch et al., 2020; Logemann et al., 2021). Our simulations thus provide a proof-of-concept for an extension of this strategy to include global biogeochemistry modeling. For the investigation of single target regions of the coastal ocean, an innovative approach including biogeochemistry was achieved by using stretched global rectilinear grids, utilizing the naturally higher resolution in the vicinity of grid poles (Gröger et al., 2013; D. Sein et al., 2015). The sediment resuspension scheme adapted for ICON-Coast, for example, was first developed for such a system (Mathis et al., 2019). The flexibility of the

767 grid generator used here (Logemann et al., 2021) also allows an assignment of increased  
768 resolution to spatially confined areas only, without the limitation of too coarse resolution in  
769 pole-distant regions that comes with stretched rectilinear grids.

770 The additional processes generalized in ICON-Coast, compared to ICON-O and its  
771 standard version of HAMOCC, are all crucially linked to the cycling of carbon and nutri-  
772 ents in the coastal ocean (Fig. 1). Tidal waves induce mixing and sediment resuspension, the  
773 aggregation of particulate matter affects vertical export fluxes, the temperature dependen-  
774 cies of remineralization and dissolution rates modify the internal recycling, and river inputs  
775 act as relevant sources of allochthonous organic and inorganic material. We evaluated these  
776 add-ons with respect to the ability of the model to simulate key physical and biogeochemical  
777 parameters influencing the surface CO<sub>2</sub> flux in the coastal ocean as well as the resulting CO<sub>2</sub>  
778 flux itself. The necessity to accurately reproduce tidal circulation, stratification, exchange  
779 flows, and sediment diagenesis for embedding coastal interface biogeochemistry in global  
780 ESMs was pointed out recently by Ward et al. (2020). Further near-term developments for  
781 ICON-Coast will primarily be related to optimization and fine tuning.

782 One of the main challenges in the model development is to bridge the dynamic scales  
783 from the deep and open ocean to the shallow shelves and marginal seas by applying globally  
784 implemented parameterizations to both eddying and non-eddying regions. ICON-Coast  
785 uses a biharmonic horizontal dissipation scheme that is dependent on the mesh spacing and  
786 thus, in combination with the regional refinement, accounts for the transition of pertinent  
787 scales. The implemented TKE vertical mixing scheme is also scale-dependent but could  
788 be further improved to better represent mixing at the bottom boundary layer as suggested  
789 e.g. by Holt et al. (2017). In the simulations, we have intentionally deactivated the eddy  
790 parameterization (Korn, 2018) because first, the combination of eddy closure with the coastal  
791 grid refinement considered here is an unsolved problem in computational fluid dynamics, and  
792 second, it allows us to better assess the impact of the grid refinement. Yet, we are optimistic  
793 that a suitably chosen eddy parameterization will lead to additional improvements of our  
794 results, in particular for the general circulation and tracer distribution in the open ocean.  
795 The sediment resuspension scheme incorporates the thickness of the bottom layer in the  
796 calculation of the sediment drag coefficient, thus accounting for the vertical grid resolution  
797 (Mathis et al., 2019). Also here, an improvement would be to include dependence on the  
798 horizontal grid scale as well.

799 Apart from a better representation of coastal carbon dynamics in ICON-Coast, higher  
800 resource demands compared to conventional global models with coarser resolution are justi-  
801 fied by the benefit of having included all coastal areas of the world within a single consistent  
802 simulation, thus naturally accounting for two-way coupling of ocean-shelf feedback mech-  
803 anisms at the global scale. Computational costs as well as data storage requirements of  
804 high-resolution simulations, though, can be substantially reduced by limiting the grid re-  
805 finement to dedicated areas only. In Table 2, we contrast resource demands for simulations  
806 with ICON-O and ICON-Coast, run on the high-res grid presented here (80-10 km) as well  
807 as on a globally uniform 10 km-resolution grid. Because of the regionally applied grid re-  
808 finement, the variable-resolution grid of ICON-Coast has less surface grid cells than the  
809 uniform-resolution grid by a factor of about 4.3. We conducted reference experiments at  
810 the current HPC system Mistral of the DKRZ, using 200 parallelized cpu nodes (see caption  
811 of Table 2 for specifications). The lower number of grid cells of the variable-resolution grid  
812 leads to a significant saving in computational cost, reducing the required real time for a  
813 simulation of 100 years with ICON-O from about 3 months to less than 1 month. The  
814 computational demands of ICON-Coast, however, increase by 25% due to the additionally  
815 implemented processes (section 2.2). About 30% of cost and time are associated with output  
816 writing, resulting in a total demand of 50 days for a 100-year simulation with ICON-Coast,  
817 including monthly 2d and 3d gridded physical and biogeochemical standard output. Sim-  
818 ilarly, the regional grid refinement reduces the storage space required for the output by a  
819 factor of about 4. These specifications of ICON-Coast allow for reasonable experimental

**Table 2:** Resource demands for simulations with ICON-O and ICON-Coast, when run on the high-res grid with variable resolution of 80-10 km as well as on a globally uniform 10 km grid. The ICON-O run on the high-res grid differs from the ICON-Coast run only with respect to the additional processes implemented to ICON-Coast (see section 2.2). All simulations are performed using 200 nodes of the HPC system 'Mistral'. Each node of the used partition consists of 2x 18-core Intel Xeon E5-2695 v4 (Broadwell) processors with a speed of 2.1 GHz. To quantify the net computing load, we give turnover rates and computational costs also for simulations excluding model output. For runs on the variable-resolution grid, this setup corresponds to an efficiency of about 0.75 and 0.85 with and without output writing, respectively, compared to linear scaling.

Metric	ICON-O uni. 10 km	ICON-O var. 80-10 km	ICON-Coast var. 80-10 km
Wet surface cells	3,730,000	860,000	860,000
Turnover (no outp.)	1.16 yr d <sup>-1</sup>	3.70 yr d <sup>-1</sup>	2.78 yr d <sup>-1</sup>
Turnover (w. outp.)	0.97 yr d <sup>-1</sup>	2.50 yr d <sup>-1</sup>	2.00 yr d <sup>-1</sup>
Cost (no outp.)	413 knh 100yr <sup>-1</sup>	128 knh 100yr <sup>-1</sup>	172 knh 100yr <sup>-1</sup>
Cost (w. outp.)	492 knh 100yr <sup>-1</sup>	192 knh 100yr <sup>-1</sup>	240 knh 100yr <sup>-1</sup>
Storage	45.9 TB 100yr <sup>-1</sup>	9.0 TB 100yr <sup>-1</sup>	11.1 TB 100yr <sup>-1</sup>

820 setups e.g. to study the anthropogenic perturbation of the marine carbon cycle, comprising  
 821 a 50-yr spinup run and two 100-yr production runs. Longer spinup simulations spanning  
 822 a few hundred years could be performed with the low-res grid configuration at comparable  
 823 total cost.

## 824 5 Conclusions

825 In this paper, we have presented ICON-Coast, the first global ocean-biogeochemistry  
 826 model that uses a telescoping high resolution for an improved representation of coastal car-  
 827 bon dynamics. This approach enables for the first time a seamless incorporation of the  
 828 global coastal ocean in model-based Earth system research. The good agreement of simu-  
 829 lated shelf-specific physical and biogeochemical processes with both observational products  
 830 and high-resolution regional modeling studies demonstrates the large potential of ICON-  
 831 Coast to be used for cross-cutting scientific applications. Linkages between carbon and  
 832 nutrient transformation pathways in the open ocean, the transition zone to the continental  
 833 shelves, and the near-coastal areas can be investigated that cannot be derived from isolated  
 834 regional modeling studies. Examples are the importance of carbon sequestration, storage,  
 835 and transport processes on the shallow shelves relative to the open ocean under different  
 836 climatic conditions (G. G. Laruelle et al., 2018), or the fate of river inputs and their con-  
 837 nection to interhemispheric carbon transport (Aumont et al., 2001; Resplandy et al., 2018).  
 838 Sensitivity experiments can be used to explore the susceptibility of the coastal ocean en-  
 839 vironment to external perturbations across a range of spatiotemporal scales and interfaces  
 840 (Ward et al., 2020).

841 The high quality of the model results shown here as well as the efficiency in compu-  
 842 tational cost and storage requirements verifies the strategy of a seamless connection of the  
 843 open and coastal ocean via regional grid refinement and enhanced process representation as  
 844 a pioneering approach for high-resolution modeling at the global scale. In view of the difficul-  
 845 ties in reconciling prognostically shelf-specific processes in the sediment, water column, and  
 846 at the air-sea interface, the model ICON-Coast, built on extended basic parameterizations  
 847 of a global ocean-biogeochemistry model, is encouraging.

848 Already with the low-res version, spanning a horizontal resolution of 160-20 km, we  
 849 achieve unprecedented accuracy and level of detail in simulating governing processes of the  
 850 coastal carbon dynamics in low, middle and high latitudes, even on the seasonal time scale.  
 851 Some features, such as the general circulation or net primary production, are comparable to

852 results from state-of-the-art high-resolution regional model systems, and the incorporation  
 853 of marine aggregates even exceeds the process representation of many established regional  
 854 ecosystem models. We thus conclude that ICON-Coast represents a new tool to deepen our  
 855 mechanistic understanding about the role of the land-ocean transition zone in the global  
 856 carbon cycle, and to narrow related uncertainties in global future projections.

857 The development of this first version of ICON-Coast was guided by the consideration  
 858 of coastal carbon dynamics. It is clear, however, that the scientific applications of such a  
 859 model system are not restricted to topics related to the carbon cycle. The concept of ICON-  
 860 Coast generally enables high-resolution modeling in the global coastal ocean, including the  
 861 continental margin as the transition to the open ocean. Potential applications thus range  
 862 from investigations of marine extreme events in coastal areas (e.g. storm surges, heat waves,  
 863 hypoxia), and ocean-shelf exchange processes including feedback mechanisms, to scenario-  
 864 based future projections of the coastal ocean physical and biogeochemical state, and sen-  
 865 sitivity studies regarding the efficiency of various coastal management and eutrophication  
 866 policies.

### 867 **Acknowledgments**

868 This work contributed to the subproject *A5 - The Land-Ocean Transition Zone* of Ger-  
 869 many's Excellence Strategy EXC 2037 *CLICCS - Climate, Climatic Change, and Society*  
 870 with project No 390683824, funded by the Deutsche Forschungsgemeinschaft (DFG, Ger-  
 871 man Research Foundation). Computational resources were made available by the German  
 872 Climate Computing Center (DKRZ) through support from the German Federal Ministry  
 873 of Education and Research (BMBF). TI was supported by the European Union's *Horizon*  
 874 *2020* research and innovation program under grant agreement No 101003536 (*ESM2025 -*  
 875 *Earth System Models for the Future*). The source code of ICON-Coast can be accessed via  
 876 the gitlab repository hosted at DKRZ: [https://gitlab.dkrz.de/icon/icon-oes/-/tree/icon-oes-](https://gitlab.dkrz.de/icon/icon-oes/-/tree/icon-oes-mm-coast_relaunch)  
 877 [mm-coast\\_relaunch](https://gitlab.dkrz.de/icon/icon-oes/-/tree/icon-oes-mm-coast_relaunch).

### 878 **References**

- 879 Aarnos, H., Gélinas, Y., Kasurinen, V., Gu, Y., Puupponen, V. M., & Vähätalo, A. V.  
 880 (2018). Photochemical Mineralization of Terrigenous DOC to Dissolved Inorganic Carbon  
 881 in Ocean. *Global Biogeochemical Cycles*, *32*, 250-266. doi: 10.1002/2017GB005698
- 882 Acha, E. A., Mianzan, H. W., Guerrero, R. A., Favero, M., & Bava, J. (2004). Marine fronts  
 883 at the continental shelves of austral South America: Physical and ecological processes.  
 884 *Journal of Marine Systems*, *44*, 83-105. doi: 10.1016/j.jmarsys.2003.09.005
- 885 Allen, J. I., Aiken, J., Anderson, T. R., Buitenhuis, E., Cornell, S., Geider, R. J., ... While,  
 886 J. (2010). Marine ecosystem models for earth systems applications: The MarQUEST  
 887 experience. *Journal of Marine Systems*, *81*, 19-33. doi: 10.1016/j.jmarsys.2009.12.017
- 888 Amiotte Suchet, P., & Probst, J. L. (1995). A global model for present-day atmospheric/soil  
 889 CO<sub>2</sub> consumption by chemical erosion of continental rocks (GEM-CO<sub>2</sub>). *Tellus B: Chem-*  
 890 *ical and Physical Meteorology*, *47*, 273-280. doi: 10.3402/tellusb.v47i1-2.16047
- 891 Araujo, M., Noriega, C., & Lefèvre, N. (2014). Nutrients and carbon fluxes in the estuaries  
 892 of major rivers flowing into the tropical Atlantic. *Front. Mar. Sci.*, *1*, 1-16. doi: 10.3389/  
 893 *fmars.2014.00010*
- 894 Arndt, S., Jørgensen, B. B., Rowe, D. E. L., Middelburg, J. J., Pancost, R. D., & Regnier,  
 895 P. (2013). Quantifying the degradation of organic matter in marine sediments: A review  
 896 and synthesis. *Earth-Science Reviews*, *123*, 53-86. doi: 10.1016/j.earscirev.2013.02.008
- 897 Arrigo, K., van Dijken, G., & Long, M. (2008). Coastal Southern Ocean: A strong anthro-  
 898 pogenic CO<sub>2</sub> sink. *Geophys. Res. Lett.*, *35*, 6 pp. doi: 10.1029/2008GL035624
- 899 Aumont, O., Orr, J. C., Monfray, P., Ludwig, W., Suchet, P. A., & Probst, J. L. (2001).  
 900 Riverine-driven interhemispheric transport of carbon. *Global Biogeochem. Cy.*, *15*, 393-  
 901 405. doi: 10.1029/1999GB001238

- 902 Babin, M., & Stramski, D. (2004). Variations in the mass-specific absorption coefficient of  
 903 mineral particles suspended in water. *Limnology and Oceanography*, *49*, 756-767. doi:  
 904 10.4319/lo.2004.49.3.0756
- 905 Bates, N. R. (2006). Air-sea CO<sub>2</sub> fluxes and the continental shelf pump of carbon in  
 906 the Chukchi Sea adjacent to the Arctic Ocean. *J. Geophys. Res.*, *111*, 21 pp. doi:  
 907 10.1029/2005JC003083
- 908 Bates, N. R., & Mathis, J. T. (2009). The Arctic Ocean marine carbon cycle: evaluation  
 909 of air-sea CO<sub>2</sub> exchanges, ocean acidification impacts and potential feedbacks. *Biogeo-*  
 910 *sciences*, *6*, 2433-2459. doi: 10.5194/bg-6-2433-2009
- 911 Bauer, J. E., Cai, W. J., Raymond, P. A., Bianchi, T. S., Hopkinson, C. S., & Regnier,  
 912 P. A. G. (2013). The changing carbon cycle of the coastal ocean. *Nature*, *504*, 61-70.  
 913 doi: 10.1038/nature12857
- 914 Becker, M., Olsen, A., Landschützer, P., Omar, A., Rehder, G., Rödenbeck, C., & Skjelvan,  
 915 I. (2021). The northern European shelf as an increasing net sink for CO<sub>2</sub>. *Biogeosciences*,  
 916 *18*, 1127-1147. doi: 10.5194/bg-18-1127-2021
- 917 Behrens, J., & Bader, M. (2009). Efficiency considerations in triangular adaptive mesh  
 918 refinement. *Phil. Trans. R. Soc. A.*, *367*, 4577-4589. doi: 10.1098/rsta.2009.0175
- 919 Berner, R. A., Lasaga, A. C., & Garrels, R. M. (1983). The carbonate-silicate geochem-  
 920 ical cycle and its effect on atmospheric carbon dioxide over the past 100 million years.  
 921 *American Journal of Science*, *283*, 641-683. doi: 10.2475/ajs.283.7.641
- 922 Beusen, A. H. W., Bouwman, A. F., Dürr, H., Dekkers, A. L. M., & Hartmann, J. (2009).  
 923 Global patterns of dissolved silica export to the coastal zone: Results from a spatially  
 924 explicit global model. *Global Biogeochem. Cy.*, *23*, GB0A02. doi: 10.1029/2008GB003281
- 925 Beusen, A. H. W., Bouwman, A. F., Van Beek, L. P. H., Mogollón, J. M., & Middelburg,  
 926 J. J. (2016). Global riverine N and P transport to ocean increased during the 20th century  
 927 despite increased retention along the aquatic continuum. *Biogeosciences*, *13*, 2441-2451.  
 928 doi: 10.5194/bg-13-2441-2016
- 929 Bianchi, A. A., Bianucci, L., Piola, A. R., Pino, D. R., Schloss, I., Poisson, A., & Balestrini,  
 930 C. F. (2005). Vertical stratification and air-sea CO<sub>2</sub> fluxes in the Patagonian shelf.  
 931 *Journal of Geophysical Research: Oceans*, *110*, 11 pp. doi: 10.1029/2004JC002488
- 932 Borges, D. B., A. V., & Frankignoulle, M. (2005). Budgeting sinks and sources of CO<sub>2</sub> in  
 933 the coastal ocean: Diversity of ecosystems counts. *Geophys. Res. Lett.*, *32*, L14601. doi:  
 934 10.1029/2005GL023053
- 935 Bourgeois, T., Orr, J. C., Resplandy, L., Terhaar, J., Ethé, C., Gehlen, M., & Bopp, L.  
 936 (2016). Coastal-ocean uptake of anthropogenic carbon. *Biogeosciences*, *13*, 4167-4185.  
 937 doi: 10.5194/bg-13-4167-2016
- 938 Boyd, P. W., Sundby, S., & Pörtner, H. O. (2014). Cross-chapter box on net primary produc-  
 939 tion in the ocean. In C. B. Field et al. (Eds.), *Climate change 2014: Impacts, adaptation,*  
 940 *and vulnerability. part a: Global and sectoral aspects. contribution of working group ii to*  
 941 *the fifth assessment report of the intergovernmental panel on climate change* (p. 133-136).  
 942 Cambridge, United Kingdom and New York, NY, USA: Cambridge University Press.
- 943 Brink, K. H. (2016). Cross-Shelf Exchange. *Annual Review of Marine Science*, *8*, 59-78.  
 944 doi: 10.1146/annurev-marine-010814-015717
- 945 Cadier, M., Gorgues, T., L'Helguen, S., Sourisseau, M., & Memery, L. (2017). Tidal cycle  
 946 control of biogeochemical and ecological properties of a macrotidal ecosystem. *Geophys.*  
 947 *Res. Lett.*, *44*, 8453-8462. doi: 10.1002/2017GL074173
- 948 Cai, W. J. (2011). Estuarine and coastal ocean carbon paradox: CO<sub>2</sub> sinks or sites of  
 949 terrestrial carbon incineration? *Ann. Rev. Mar. Sci.*, *3*, 123-145. doi: 10.1146/annurev-  
 950 -marine-120709-142723
- 951 Cai, W. J., Chen, L., Chen, B., Gao, Z., Lee, S. H., Chen, J., ... Zhang, H. (2010). Decrease  
 952 in the CO<sub>2</sub> Uptake Capacity in an Ice-Free Arctic Ocean Basin. *Science*, *329*, 556-559.  
 953 doi: 10.1126/science.1189338
- 954 Canadell, J. G., Ciais, P., Dhakal, S., Dolman, H., Friedlingstein, P., Gurney, K. R., ...  
 955 Raupach, M. R. (2010). Interactions of the carbon cycle, human activity, and the climate

- 956 system: a research portfolio. *Current Opinion in Environmental Sustainability*, 2, 301-  
 957 311. doi: 10.1016/j.cosust.2010.08.003
- 958 Cao, Z., Yang, W., Zhao, Y., Guo, X., Yin, Z., Du, C., ... Dai, M. (2020). Diagnosis of  
 959 CO<sub>2</sub> dynamics and fluxes in global coastal oceans. *National Science Review*, 7, 786-797.  
 960 doi: 10.1093/nsr/nwz105
- 961 Carreto, J. I., Montoya, N. G., Carignan, M. O., Akselman, R., Acha, E. M., & Derisio,  
 962 C. (2016). Environmental and biological factors controlling the spring phytoplankton  
 963 bloom at the Patagonian shelf-break front - Degraded fucoxanthin pigments and the  
 964 importance of microzooplankton grazing. *Progress in Oceanography*, 146, 1-21. doi:  
 965 10.1016/j.pocean.2016.05.002
- 966 Chen, C., Liu, H., & Beardsley, R. C. (2003). An unstructured grid, finite-volume, three-  
 967 dimensional, primitive equations ocean model: Application to coastal ocean and estu-  
 968 aries. *Journal of Atmospheric and Oceanic Technology*, 20, 159-186. doi: 10.1175/  
 969 1520-0426(2003)020<0159:AUGFVT>2.0.CO;2
- 970 Cheng, Y., Putrasahan, D., Beal, L., & Kirtman, B. (2016). Quantifying Agulhas Leakage  
 971 in a High-Resolution Climate Model. *Journal of Climate*, 29, 6881-6892. doi: 10.1175/  
 972 JCLI-D-15-0568.1
- 973 Combes, V., & Matano, R. P. (2018). The Patagonian shelf circulation: Drivers and  
 974 variability. *Progress in Oceanography*, 167, 24-43.
- 975 Combes, V., Matano, R. P., & Palma, E. D. (2021). Circulation and cross-shelf exchanges in  
 976 the northern shelf region of the southwestern Atlantic: Kinematics. *Journal of Geophysical*  
 977 *Research: Oceans*, 126, 16 pp. doi: 10.1029/2020JC016959
- 978 Compton, J., Mallinson, D., Glenn, C. R., Filippelli, G., Follmi, K., Shields, G., & Zanin, Y.  
 979 (2000). Variations in the Global Phosphorus cycle. In *Marine authigenesis: From global*  
 980 *to microbial*. SEPM Society for Sedimentary Geology. doi: 10.2110/pec.00.66.0021
- 981 Dai, M., Cao, Z., Guo, X., Zhai, W., Liu, Z., Yin, Z., ... Du, C. (2013). Why are some  
 982 marginal seas sources of atmospheric CO<sub>2</sub>? *Geophysical Research Letters*, 40, 2154-2158.  
 983 doi: doi.org/10.1002/grl.50390
- 984 Dale, A. C., & Inall, M. E. (2015). Tidal mixing processes amid small-scale, deep-ocean  
 985 topography. *Geophysical Research Letters*, 42, 484-491. doi: 10.1002/2014GL062755
- 986 Danilov, S. (2010). On utility of triangular C-grid type discretization for numerical modeling  
 987 of large-scale ocean flows. *Ocean Dynamics*, 60, 1361-1369. doi: 10.1007/s10236-010-0339  
 988 -6
- 989 Danilov, S., Wang, Q., Timmermann, R., Iakovlev, N., Sidorenko, D., Kimmritz, M., ...  
 990 Schröter, J. (2015). Finite-element sea ice model (FESIM), version 2. *Geosci. Model*  
 991 *Dev.*, 8, 1747-1761. doi: 10.5194/gmd-8-1747-2015
- 992 Dee, D. P., Uppala, S. M., Simmons, A. J., Berrisford, P., Poli, P., Kobayashi, S., ...  
 993 Vitart, F. (2011). The ERA-Interim reanalysis: configuration and performance of the  
 994 data assimilation system. *Quarterly Journal of the Royal Meteorological Society*, 137,  
 995 553-597. doi: 10.1002/qj.828
- 996 de Souza, M. M., Mathis, M., Mayer, B., Noernberg, M. A., & Pohlmann, T. (2020).  
 997 Possible impacts of anthropogenic climate change to the upwelling in the South Brazil  
 998 Bight. *Climate Dynamics*, 55, 651-664. doi: 10.1007/s00382-020-05289-0
- 999 Diesing, M., Kröger, S., Parker, R., Jenkins, C., Mason, C., & Weston, K. (2017). Predicting  
 1000 the standing stock of organic carbon in surface sediments of the North-West European  
 1001 continental shelf. *Biogeochemistry*, 135, 183-200. doi: 10.1007/s10533-017-0310-4
- 1002 Diesing, T. T., M., & Bjarnadóttir, L. R. (2021). Organic carbon densities and accumulation  
 1003 rates in surface sediments of the North Sea and Skagerrak. *Biogeosciences*, 18, 2139-2160.  
 1004 doi: 10.5194/bg-18-2139-2021
- 1005 Dixit, S., van Cappellen, P., & van Bennekom, A. J. (2001). Processes controlling solubility  
 1006 of biogenic silica and pore water build-up of silicic acid in marine sediments. *Marine*  
 1007 *Chemistry*, 73, 333-352. doi: 10.1016/S0304-4203(00)00118-3
- 1008 Dürr, H. H., Meybeck, M., Hartmann, J., Laruelle, G. G., & Roubex, V. (2011). Global  
 1009 spatial distribution of natural riverine silica inputs to the coastal zone. *Biogeosciences*,

- 1010 8, 597-620. doi: 10.5194/bg-8-597-2011
- 1011 Egbert, G. D., & Erofeeva, S. Y. (2002). Efficient inverse modeling of barotropic ocean  
1012 tides. *J. Atmos. Ocean. Technol.*, *19*, 183-204. doi: 10.1175/1520-0426(2002)019(0183:  
1013 EIMOBO)2.0.CO;2
- 1014 Ekici, A., Beer, C., Hagemann, S., Boike, J., Langer, M., & Hauck, C. (2014). Simulating  
1015 high-latitude permafrost regions by the JSBACH terrestrial ecosystem model. *Geoscientific Model Development*, *7*, 631-647. doi: 10.5194/gmd-7-631-2014
- 1016  
1017 Eyring, V., Bony, S., Meehl, G. A., Senior, C. A., Stevens, B., Stouffer, R. J., & Taylor,  
1018 K. E. (2016). Overview of the coupled model intercomparison project phase 6 (CMIP6)  
1019 experimental design and organization. *Geoscient. Model. Dev.*, *9*, 1937-1958. doi: 10  
1020 .5194/gmd-9-1937-2016
- 1021 Fennel, K., Alin, S., Barbero, L., Evans, W., Bourgeois, T., Cooley, S., ... Wang, Z. A.  
1022 (2019). Carbon cycling in the North American coastal ocean: a synthesis. *Biogeosciences*,  
1023 *16*, 1281-1304. doi: 10.5194/bg-16-1281-2019
- 1024 Fettweis, M., Baeye, M., Van der Zande, D., Van den Eynde, D., & Lee, B. J. (2014).  
1025 Seasonality of flocculation strength in the southern North Sea. *Journal of Geophysical Research:  
1026 Oceans*, *119*, 1911-1926. doi: 10.1002/2013JC009750
- 1027 Fichot, C. G., & Benner, R. (2014). The fate of terrigenous dissolved organic carbon in a  
1028 river-influenced ocean margin. *Global Biogeochemical Cycles*, *28*, 300-318. doi: 10.1002/  
1029 2013GB004670
- 1030 Franco, B. C., Palma, E. D., Combes, V., & Lasta, M. L. (2017). Physical processes  
1031 controlling passive larval transport at the Patagonian Shelf Break Front. *Journal of Sea  
1032 Research*, *124*, 17-25. doi: 10.1016/j.seares.2017.04.012
- 1033 Francois, R., Honjo, S., Krishfield, R., & Manganini, S. (2002). Factors controlling the flux  
1034 of organic carbon to the bathypelagic zone of the ocean. *Global Biogeochemical Cycles*,  
1035 *16*, 20 pp. doi: 10.1029/2001GB001722
- 1036 Franzo, A., Celussi, M., Bazzaro, M., Relitti, F., & Negro, P. D. (2019). Microbial processing  
1037 of sedimentary organic matter at a shallow LTER site in the northern Adriatic Sea: an  
1038 8-year case study. *Nature Conservation*, *34*, 397-415. doi: 10.3897/natureconservation  
1039 .34.30099
- 1040 Friedlingstein, P., O'Sullivan, M., Jones, M. W., Andrew, R. M., Hauck, J., Olsen, A.,  
1041 ... Zaehle, S. (2020). Global Carbon Budget 2020. *Earth System Science Data*, *12*,  
1042 3269-3340. doi: 10.5194/essd-12-3269-2020
- 1043 Galy, V., Peucker-Ehrenbrink, B., & Eglinton, T. (2015). Global carbon export from  
1044 the terrestrial biosphere controlled by erosion. *Nature*, *521*, 204-207. doi: 10.1038/  
1045 nature14400
- 1046 Gaspar, P., Grégoris, Y., & Lefevre, J. M. (1990). A simple eddy kinetic energy model for  
1047 simulations of the oceanic vertical mixing: Tests at station Papa and long-term upper  
1048 ocean study site. *Journal of Geophysical Research: Oceans*, *95*, 16179-16193. doi: 10  
1049 .1029/JC095iC09p16179
- 1050 Gattuso, J. P., Frankignoulle, M., & Wollast, R. (1998). Carbon and carbonate metabolism  
1051 in coastal aquatic ecosystems. *Annual Review of Ecology and Systematics*, *29*, 405-434.  
1052 doi: 10.1146/annurev.ecolsys.29.1.405
- 1053 Gille, S. T., Metzger, E. J., & Tokmakian, R. (2004). Seafloor topography and ocean  
1054 circulation. *Oceanography*, *17*, 47-54. doi: 10.5670/oceanog.2004.66
- 1055 Gloege, L., McKinley, G. A., Mouw, C. B., & Ciochetto, A. B. (2017). Global evaluation of  
1056 particulate organic carbon flux parameterizations and implications for atmospheric pCO<sub>2</sub>.  
1057 *Global Biogeochem. Cycles*, *31*, 1192-1215. doi: 10.1002/2016GB005535
- 1058 Gonçalves-Araujo, R., de Souza, M. S., Mendes, C. R. B., Tavano, V. M., & Garcia, C. A. E.  
1059 (2016). Seasonal change of phytoplankton (spring vs. summer) in the southern Patagonian  
1060 shelf. *Continental Shelf Research*, *124*, 142-152. doi: 10.1016/j.csr.2016.03.023
- 1061 Graham, J. A., O'Dea, E., Holt, J., Polton, J., Hewitt, H. T., Furner, R., ... May-  
1062 orga Adame, C. G. (2018a). AMM15: a new high resolution NEMO configuration for  
1063 operational simulation of the European north-west shelf. *Geoscientific Model Develop-*

- 1064        *ment*, *11*, 681-696. doi: 10.5194/gmd-11-681-2018
- 1065        Graham, J. A., Rosser, J. P., O’Dea, E., & Hewitt, H. T. (2018b). Resolving Shelf Break Ex-  
1066        change Around the European Northwest Shelf. *Geophysical Research Letters*, *45*, 12386-  
1067        12395.
- 1068        Gregor, L., Lebehot, A. D., Kok, S., & Scheel Monteiro, P. M. (2019). A comparative  
1069        assessment of the uncertainties of global surface ocean CO<sub>2</sub> estimates using a machine-  
1070        learning ensemble (CSIR-ML6 version 2019a) – have we hit the wall? *Geoscientific Model*  
1071        *Development*, *12*, 5113-5136. doi: 10.5194/gmd-12-5113-2019
- 1072        Gröger, M., Maier-Reimer, E., Mikolajewicz, U., Moll, A., & Sein, D. (2013). NW Euro-  
1073        pean shelf under climate warming: implications for open ocean - shelf exchange, primary  
1074        production, and carbon absorption. *Biogeosciences*, *10*, 3767-3792.
- 1075        Gruber, N. (2015). Ocean biogeochemistry: Carbon at the coastal interface. *Nature*,  
1076        *517*(7533), 148-149. doi: 10.1038/nature14082
- 1077        Guidi, L., Legendre, L., Reygondeau, G., Uitz, J., Stemann, L., & Henson, S. A. (2015). A  
1078        new look at ocean carbon remineralization for estimating deepwater sequestration. *Global*  
1079        *Biogeochem. Cycles*, *29*, 1044-1059. doi: 10.1002/2014GB005063
- 1080        Guihou, K., Piola, A. R., Palma, E. D., & Chidichimo, M. P. (2020). Dynamical con-  
1081        nections between large marine ecosystems of austral South America based on numerical  
1082        simulations. *Ocean Science*, *16*, 271-290. doi: 10.5194/os-16-271-2020
- 1083        Guihou, K., Polton, J., Harle, J., Wakelin, S., O’Dea, E., & Holt, J. (2018). Kilometric Scale  
1084        Modeling of the North West European Shelf Seas: Exploring the Spatial and Temporal  
1085        Variability of Internal Tides. *Journal of Geophysical Research: Oceans*, *123*, 688-707.  
1086        doi: 10.1002/2017JC012960
- 1087        Gutjahr, O., Brüggemann, N., Haak, H., Jungclaus, J., Putrasahan, D., Lohmann, K., &  
1088        von Storch, J. (2021). Comparison of ocean vertical mixing schemes in the Max Planck  
1089        Institute Earth System Model (MPI-ESM1.2). *Geophysical Model Development*, *14*, 2317-  
1090        2349. doi: 10.5194/gmd-14-2317-2021
- 1091        Hagemann, S., & Dümenil-Gates, L. (2001). Validation of the hydrological cycle of ECMWF  
1092        and NCEP reanalyses using the MPI hydrological discharge model. *Journal of Geophysical*  
1093        *Research - Atmospheres*, *106*, 1503-1510.
- 1094        Hagemann, S., Stacke, T., & Ho-Hagemann, H. T. M. (2020). High Resolution Discharge  
1095        Simulations Over Europe and the Baltic Sea Catchment. *Frontiers in Earth Science*, *8*,  
1096        12 pp. doi: 10.3389/feart.2020.00012
- 1097        Hallberg, R. (2013). Using a resolution function to regulate parameterizations of oceanic  
1098        mesoscale eddy effects. *Ocean Modelling*, *72*, 92-103. doi: 10.1016/j.ocemod.2013.08.007
- 1099        Hartmann, J., Jansen, N., Dürr, H. H., Kempe, S., & Köhler, P. (2009). Global CO<sub>2</sub>-  
1100        consumption by chemical weathering: What is the contribution of highly active weathering  
1101        regions? *Global and Planetary Change*, *69*, 185-194. doi: 10.1016/j.gloplacha.2009.07  
1102        .007
- 1103        Hátún, H., Azetsu-Scott, K., Somavilla, R., Rey, F., Johnson, C., Mathis, M., ... Ólafsson,  
1104        J. (2017). The subpolar gyre regulates silicate concentrations in the North Atlantic.  
1105        *Scientific Reports*, *7*(14576), 9 pp.
- 1106        Hauck, J., Zeising, M., Quéré, C. L., Gruber, N., Bakker, D. C. E., Bopp, L., ... Séférian,  
1107        R. (2020). Consistency and Challenges in the Ocean Carbon Sink Estimate for the Global  
1108        Carbon Budget. *Frontiers in Marine Science*, *7*, 22 pp. doi: 10.3389/fmars.2020.571720
- 1109        Heinze, C., Maier-Reimer, E., Winguth, A. M. E., & Archer, D. (1999). A global oceanic  
1110        sediment model for long-term climate studies. *Global Biogeochem. Cycles*, *13*, 221-250.
- 1111        Hewitt, H. T., Bell, M. J., Chassignet, E. P., Czaja, A., Ferreira, D., Griffies, S. M., ...  
1112        Roberts, M. J. (2017). Will high-resolution global ocean models benefit coupled pre-  
1113        dictions on short-range to climate timescales? *Ocean Modelling*, *120*, 120-136. doi:  
1114        10.1016/j.ocemod.2017.11.002
- 1115        Hewitt, H. T., Roberts, M., Mathiot, P., Biastoch, A., Blockley, E., Chassignet, E. P., ...  
1116        Zhang, Q. (2020). Resolving and Parameterising the Ocean Mesoscale in Earth System  
1117        Models. *Curr. Clim. Change Rep.*, *6*, 137-152. doi: 10.1007/s40641-020-00164-w

- 1118 Hoch, K. E., Petersen, M. R., Brus, S. R., Engwirda, D., Roberts, A. F., Rosa, K. L., &  
 1119 Wolfram, P. J. (2020). MPAS-Ocean Simulation Quality for Variable-Resolution North  
 1120 American Coastal Meshes. *Journal of Advances in Modeling Earth Systems*, *12*, 23 pp.  
 1121 doi: 10.1029/2019MS001848
- 1122 Holt, J., Butenschön, M., Wakelin, S. L., Artioli, Y., & Allen, J. I. (2012). Oceanic  
 1123 controls on the primary production of the northwest European continental shelf: model  
 1124 experiments under recent past conditions and a potential future scenario. *Biogeosciences*,  
 1125 *9*(1), 97-117.
- 1126 Holt, J., Harle, J., Proctor, R., Michel, S., Ashworth, M., Batstone, C., ... Smith, G.  
 1127 (2009). Modelling the global coastal ocean. *Philosophical Transactions of the Royal  
 1128 Society A: Mathematical, Physical and Engineering Sciences*, *367*, 939-951. doi: 10.1098/  
 1129 rsta.2008.0210
- 1130 Holt, J., Hyder, P., Ashworth, M., Harle, J., Hewitt, H. T., Liu, H., ... Wood, R. (2017).  
 1131 Prospects for improving the representation of coastal and shelf seas in global ocean models.  
 1132 *Geoscientific Model Development*, *10*, 499-523. doi: 10.5194/gmd-10-499-2017
- 1133 Holt, J., & Proctor, R. (2008). The seasonal circulation and volume transport on the  
 1134 northwest European continental shelf: A fine-resolution model study. *J. Geophys. Res.*,  
 1135 *113*, 20 pp. doi: 10.1029/2006JC004034
- 1136 Holt, J., Schrum, C., Cannaby, H., Daewel, U., Allen, I., Artioli, Y., ... Wakelin, S. (2016).  
 1137 Potential impacts of climate change on the primary production of regional seas: A com-  
 1138 parative analysis of five European seas. *Progress in Oceanography*, *140*, 91-115.
- 1139 Hu, L. M., Lin, T., Shi, X. F., Yang, Z. S., Wang, H. J., Zhang, G., & Guo, Z. G. (2011). The  
 1140 role of shelf mud depositional process and large river inputs on the fate of organochlorine  
 1141 pesticides in sediments of the Yellow and East China seas. *Geophysical Research Letters*,  
 1142 *38*, 6 pp. doi: 10.1029/2010GL045723
- 1143 Huang, W. J., Cai, W. J., Wang, Y., Lohrenz, S. E., & Murrell, M. C. (2015). The carbon  
 1144 dioxide system on the Mississippi River-dominated continental shelf in the northern Gulf  
 1145 of Mexico: 1. Distribution and air-sea CO<sub>2</sub> flux. *Journal of Geophysical Research: Oceans*,  
 1146 *120*, 1429-1445. doi: 10.1002/2014JC010498
- 1147 Hurd, D. C. (1972). Factors affecting solution rate of biogenic opal in seawater. *Earth and  
 1148 Planetary Science Letters*, *15*, 411-417. doi: 10.1016/0012-821X(72)90040-4
- 1149 Ilyina, T., Six, K. D., Segschneider, J., Maier-Reimer, E., Li, H., & Núñez-Riboni, I. (2013).  
 1150 The global ocean biogeochemistry model HAMOCC: Model architecture and performance  
 1151 as component of the MPI-Earth System Model in different CMIP5 experimental realiza-  
 1152 tions. *Journal of Advances in Modeling Earth Systems*, *5*, 287-315.
- 1153 Jiao, N., Liang, Y., Zhang, Y., Liu, J., Zhang, Y., Zhang, R., ... Zhang, S. (2018). Carbon  
 1154 pools and fluxes in the China Seas and adjacent oceans. *Science China Earth Sciences*,  
 1155 *61*, 1535-1563. doi: 10.1007/s11430-018-9190-x
- 1156 Kahl, L. C., Bianchi, A. A., Osiroff, A. P., Pino, D. R., & Piola, A. R. (2017). Distribution  
 1157 of sea-air CO<sub>2</sub> fluxes in the Patagonian Sea: Seasonal, biological and thermal effects.  
 1158 *Continental Shelf Research*, *143*, 18-28. doi: 10.1016/j.csr.2017.05.011
- 1159 Kaiser, K., Benner, R., & W., A. R. M. (2017). The fate of terrigenous dissolved organic  
 1160 carbon on the Eurasian shelves and export to the North Atlantic. *Scientific Reports*, *7*,  
 1161 11 pp. doi: 10.1038/s41598-017-12729-1
- 1162 Kamatani, A. (1982). Dissolution rates of silica from diatoms decomposing at various  
 1163 temperatures. *Marine Biology*, *68*, 91-96. doi: 10.1007/BF00393146
- 1164 Kämpf, J. (2021). On the upslope sediment transport at continental margins. *Journal of  
 1165 Marine Systems*, *219*, 103546. doi: 10.1016/j.jmarsys.2021.103546
- 1166 Kandasamy, S., & Nath, B. N. (2016). Perspectives on the Terrestrial Organic Matter  
 1167 Transport and Burial along the Land-Deep Sea Continuum: Caveats in Our Understand-  
 1168 ing of Biogeochemical Processes and Future Needs. *Front. Mar. Sci.*, *3*, 18 pp. doi:  
 1169 10.3389/fmars.2016.00259
- 1170 Karakaş, G., Nowald, N., Blaas, M., Marchesiello, P., Frickenhaus, S., & Schlitzer, R. (2006).  
 1171 High-resolution modeling of sediment erosion and particle transport across the northwest

- 1172 African shelf. *J. Geophys. Res.*, *111*, 13 pp. doi: 10.1029/2005JC003296
- 1173 Kartadikaria, A. R., Watanabe, A., Nadaoka, K., Adi, N. S., Prayitno, H. B., Soemo-
- 1174 rumekso, S., ... Khasanah, E. N. (2015). CO<sub>2</sub> sink/source characteristics in the trop-
- 1175 ical Indonesian seas. *Journal of Geophysical Research: Oceans*, *120*, 7842-7856. doi:
- 1176 10.1002/2015JC010925
- 1177 Kastner, S. E., Horner-Devine, A. R., & Thomson, J. (2018). The influence of wind
- 1178 and waves on spreading and mixing in the Fraser River plume. *Journal of Geophysical*
- 1179 *Research: Oceans*, *123*, 6818-6840. doi: 10.1029/2018JC013765
- 1180 Kealoha, A. K., Shamberger, K. E. F., DiMarco, S. F., Thyng, K. M., Hetland, R. D.,
- 1181 Manzello, D. P., ... Enochs, I. C. (2020). Surface Water CO<sub>2</sub> variability in the Gulf of
- 1182 Mexico (1996-2017). *Scientific Reports*, *10*, 13 pp. doi: 10.1038/s41598-020-68924-0
- 1183 Kerimoglu, O., Voynova, Y. G., Chegini, F., Brix, H., Callies, U., Hofmeister, R., ... van
- 1184 Beusekom, J. E. E. (2020). Interactive impacts of meteorological and hydrological condi-
- 1185 tions on the physical and biogeochemical structure of a coastal system. *Biogeosciences*,
- 1186 *17*, 5097-5127. doi: 10.5194/bg-17-5097-2020
- 1187 Kitidis, V., Shutler, J. D., Ashton, I., Warren, M., Brown, I., Findlay, H., ... Nightingale,
- 1188 P. D. (2019). Winter weather controls net influx of atmospheric CO<sub>2</sub> on the north-west
- 1189 European shelf. *Scientific Reports*, *9*, 11 pp. doi: 10.1038/s41598-019-56363-5
- 1190 Kloster, S., Feichter, J., Maier-Reimer, E., Six, K. D., Stier, P., & Wetzol, P. (2006). DMS
- 1191 cycle in the marine ocean-atmosphere system - A global model study. *Biogeosciences*, *3*,
- 1192 29-51.
- 1193 Korn, P. (2017). Formulation of an unstructured grid model for global ocean dynamics. *J.*
- 1194 *Comput. Phys.*, *339*, 525-552. doi: 10.1016/j.jcp.2017.03.009
- 1195 Korn, P. (2018). A structure-preserving discretization of ocean parametrizations on un-
- 1196 structured grids. *Ocean Modelling*, *132*, 73-90. doi: 10.1016/j.ocemod.2018.10.002
- 1197 Korn, P., & Linardakis, L. (2018). A conservative discretization of the shallow-water
- 1198 equations on triangular grids. *J. Comput. Phys.*, *375*, 871-900. doi: 10.1016/j.jcp
- 1199 .2018.09.002
- 1200 Koul, V., Schrum, C., Düsterhus, A., & Baehr, J. (2019). Atlantic Inflow to the North Sea
- 1201 Modulated by the Subpolar Gyre in a Historical Simulation With MPI-ESM. *Journal of*
- 1202 *Geophysical Research: Oceans*, *124*, 1807-1826. doi: 10.1029/2018JC014738
- 1203 Krumins, V., Gehlen, M., Arndt, S., Cappellen, P. V., & Regnier, P. (2013). Dissolved
- 1204 inorganic carbon and alkalinity fluxes from coastal marine sediments: model estimates
- 1205 for different shelf environments and sensitivity to global change. *Biogeosciences*, *10*,
- 1206 371-398. doi: 10.5194/bg-10-371-2013
- 1207 Kühn, W., Pätsch, J., Thomas, H., Borges, A. V., Schiettecatte, L.-S., Bozec, Y., & Prowe,
- 1208 A. E. F. (2010). Nitrogen and carbon cycling in the North Sea and exchange with the
- 1209 North Atlantic - A model study, Part II: Carbon budget and fluxes. *Continental Shelf*
- 1210 *Research*, *30*, 1701-1716.
- 1211 Kulk, G., Platt, T., Dingle, J., Jackson, T., Jönsson, B. F., Bouman, H. A., ... Sathyen-
- 1212 dranath, S. (2020). Primary Production, an Index of Climate Change in the Ocean:
- 1213 Satellite-Based Estimates over Two Decades. *Remote Sensing*, *12*, 27 pp. doi: 10.3390/
- 1214 rs12050826
- 1215 Kwon, E. Y., Primeau, F., & Sarmiento, J. L. (2009). The impact of remineralization depth
- 1216 on the air-sea carbon balance. *Nature Geoscience*, *2*, 630-635. doi: 10.1038/ngeo612
- 1217 Lacroix, F., Ilyina, T., & Hartmann, J. (2020). Oceanic CO<sub>2</sub> outgassing and biological
- 1218 production hotspots induced by pre-industrial river loads of nutrients and carbon in a
- 1219 global modeling approach. *Biogeosciences*, *17*, 55-88. doi: 10.5194/bg-17-55-2020
- 1220 Lacroix, F., Ilyina, T., Laruelle, G. G., & Regnier, P. (2021a). Reconstructing the Preindus-
- 1221 trial Coastal Carbon Cycle Through a Global Ocean Circulation Model: Was the Global
- 1222 Continental Shelf Already Both Autotrophic and a CO<sub>2</sub> Sink? *Global Biogeochemical*
- 1223 *Cycles*, *35*, e2020GB006603. doi: 10.1029/2020GB006603
- 1224 Lacroix, F., Ilyina, T., Mathis, M., Laruelle, G. G., & Regnier, P. (2021b). Historical
- 1225 Increases in Land-Derived Nutrient Inputs May Alleviate Effects of a Changing Physical

- 1226 Climate on the Oceanic Carbon Cycle. *Global Change Biology*, in press. doi: 10.1111/  
1227 gcb.15822
- 1228 Landschützer, P., Gruber, N., & Bakker, D. C. E. (2016). Decadal variations and trends  
1229 of the global ocean carbon sink. *Global Biogeochemical Cycles*, *30*, 1396-1417. doi:  
1230 10.1002/2015GB005359
- 1231 Laruelle, G., Lauerwald, R., Pfeil, B., & Regnier, P. (2014). Regionalized global budget of  
1232 the CO<sub>2</sub> exchange at the air-water interface in continental shelf seas. *Global Biogeochem-  
1233 ical Cycles*, *28*(11), 1199-1214. doi: 10.1002/2014GB004832
- 1234 Laruelle, G. G., Cai, W. J., Hu, X., Gruber, N., Mackenzie, F. T., & Regnier, P. (2018).  
1235 Continental shelves as a variable but increasing global sink for atmospheric carbon dioxide.  
1236 *Nature Communications*, *9*, 11 pp. doi: 10.1038/s41467-017-02738-z
- 1237 Laruelle, G. G., Dürr, H. H., Slomp, C. P., & Borges, A. V. (2010). Evaluation of sinks  
1238 and sources of CO<sub>2</sub> in the global coastal ocean using a spatially-explicit typology of  
1239 estuaries and continental shelves. *Geophysical Research Letters*, *37*, L15607. doi: 10.1029/  
1240 2010GL043691
- 1241 Laufkötter, C., John, J. G., Stock, C. A., & Dunne, J. P. (2017). Temperature and oxygen  
1242 dependence of the remineralization of organic matter. *Global Biogeochem. Cycles*, *31*,  
1243 1038-1050. doi: 10.1002/2017GB005643
- 1244 Laufkötter, C., Vogt, M., Gruber, N., Aita-Noguchi, M., Aumont, O., Bopp, L., ... Völker,  
1245 C. (2015). Drivers and uncertainties of future global marine primary production in marine  
1246 ecosystem models. *Biogeosciences*, *12*, 6955-6984. doi: 10.5194/bg-12-6955-2015
- 1247 Lavelle, J. W., Thurnherr, A. M., Mullineaux, L. S., McGillicuddy, D. J., & Ledwell, J. R.  
1248 (2012). The Prediction, Verification, and Significance of Flank Jets at Mid-Ocean Ridges.  
1249 *Oceanography*, *25*, 277-283.
- 1250 Lee, T. R., Wood, W. T., & Phrampus, B. J. (2019). A Machine Learning (kNN) Approach  
1251 to Predicting Global Seafloor Total Organic Carbon. *Global Biogeochemical Cycles*, *33*,  
1252 37-46. doi: 10.1029/2018GB005992
- 1253 Legge, O., Johnson, M., Hicks, N., Jickells, T., Diesing, M., Aldridge, J., ... Williamson,  
1254 P. (2020). Carbon on the Northwest European Shelf: Contemporary Budget and Future  
1255 Influences. *Frontiers in Marine Science*, *7*, 23 pp. doi: 10.3389/fmars.2020.00143
- 1256 Lemmen, C. (2018). North Sea Ecosystem-Scale Model-Based Quantification of Net Primary  
1257 Productivity Changes by the Benthic Filter Feeder *Mytilus edulis*. *Water*, *10*, 18 pp. doi:  
1258 10.3390/w10111527
- 1259 Li, G., Gao, P., Wang, F., & Liang, Q. (2004). Estimation of ocean primary productivity  
1260 and its spatio-temporal variation mechanism for East China Sea based on VGPM model.  
1261 *Journal of Geographical Sciences*, *14*, 32-40. doi: 10.1007/BF02873088
- 1262 Li, M., Peng, C., Wang, M., Xue, W., Zhang, K., Wang, K., ... Zhu, Q. (2017). The  
1263 carbon flux of global rivers: A re-evaluation of amount and spatial patterns. *Ecological  
1264 Indicators*, *80*, 40-51. doi: 10.1016/j.ecolind.2017.04.049
- 1265 Li, M., Peng, C., Zhou, X., Yang, Y., Guo, Y., Shi, G., & Zhu, Q. (2019). Modeling Global  
1266 Riverine DOC Flux Dynamics From 1951 to 2015. *Journal of Advances in Modeling Earth  
1267 Systems*, *11*, 514-530. doi: 10.1029/2018MS001363
- 1268 Li, Z., von Storch, J. S., & Müller, M. (2017). The K1 internal tide simulated by a 1/10°  
1269 OGCM. *Ocean Modelling*, *113*, 145-156. doi: 10.1016/j.ocemod.2017.04.002
- 1270 Lie, H. J., & Cho, C. H. (2016). Seasonal circulation patterns of the Yellow and East  
1271 China Seas derived from satellite-tracked drifter trajectories and hydrographic observa-  
1272 tions. *Progress in Oceanography*, *146*, 121-141. doi: 10.1016/j.pocean.2016.06.004
- 1273 Liu, F., Su, J., Moll, A., Krasemann, H., X. Chen, T. P., & Wirtz, K. (2014). Assessment  
1274 of the summer-autumn bloom in the Bohai Sea using satellite images to identify the roles  
1275 of wind mixing and light conditions. *Journal of Marine Systems*, *129*, 303-317. doi:  
1276 10.1016/j.jmarsys.2013.07.007
- 1277 Liu, X., Dunne, J. P., Stock, C. A., Harrison, M. J., Adcroft, A., & Resplandy, L. (2019).  
1278 Simulating Water Residence Time in the Coastal Ocean: A Global Perspective. *Geophys-  
1279 ical Research Letters*, *46*, 13910-13919. doi: 10.1029/2019GL085097

- 1280 Liu, Z., & Gan, J. (2016). Open boundary conditions for tidally and subtidally forced  
1281 circulation in a limited-area coastal model using the Regional Ocean Modeling System  
1282 (ROMS). *Journal of Geophysical Research: Oceans*, *121*, 6184-6203. doi: 10.1002/  
1283 2016JC011975
- 1284 Locarnini, R. A., Mishonov, A. V., Antonov, J. I., Boyer, T. P., Garcia, H. E., Baranova,  
1285 O. K., ... Seidov, D. (2013). World Ocean Atlas 2013, Volume 1: Temperature. *Levitus,*  
1286 *S., Mishonov, A. (Eds.), NOAA Atlas NESDIS, 73*, 40 pp.
- 1287 Loebel, M., Colijn, F., van Beusekom, J. E. E., Baretta-Bekker, J. G., Lancelot, C., Philip-  
1288 part, C. J. M., ... Wiltshire, K. H. (2009). Recent patterns in potential phytoplankton  
1289 limitation along the Northwest European continental coast. *Journal of Sea Research*, *61*,  
1290 34-43. doi: 10.1016/j.seares.2008.10.002
- 1291 Logemann, K., Linardakis, L., Korn, P., & Schrum, C. (2021). Global tide simulations with  
1292 ICON-O: testing the model performance on highly irregular meshes. *Ocean Dynamics*,  
1293 *71*, 43-57. doi: 10.1007/s10236-020-01428-7
- 1294 Lønborg, C., Álvarez Salgado, X. A., Letscher, R. T., & Hansell, D. A. (2018). Large  
1295 Stimulation of Recalcitrant Dissolved Organic Carbon Degradation by Increasing Ocean  
1296 Temperatures. *Front. Mar. Sci.*, *4*, 11 pp. doi: 10.3389/fmars.2017.00436
- 1297 Luisetti, T., Ferrini, S., Grilli, G., Jickells, T. D., Kennedy, H., Kröger, S., ... Tyllianakis,  
1298 E. (2020). Climate action requires new accounting guidance and governance frameworks  
1299 to manage carbon in shelf seas. *Nature Communications*, *11*, 4599. doi: 10.1038/s41467-  
1300 -020-18242-w
- 1301 Luo, X. (2014). Phytoplankton community and primary productivity in the Yellow Sea and  
1302 East China Sea. In *Marine biodiversity and ecosystem dynamics of the northwest pacific*  
1303 *ocean* (p. 13 pp). Science Press Beijing.
- 1304 Maerz, J., Hofmeister, R., van der Lee, E. M., Gräwe, U., Riethmüller, R., & Wirtz, K. W.  
1305 (2016). Maximum sinking velocities of suspended particulate matter in a coastal transition  
1306 zone. *Biogeosciences*, *13*, 4863-4876. doi: 10.5194/bg-13-4863-2016
- 1307 Maerz, J., Six, K. D., Stemmler, I., Ahmerkamp, S., & Ilyina, T. (2020). Microstructure  
1308 and composition of marine aggregates as co-determinants for vertical particulate organic  
1309 carbon transfer in the global ocean. *Biogeosciences*, *17*, 1765-1803. doi: 10.5194/bg-17-  
1310 -1765-2020
- 1311 Maier-Reimer, E., Kriest, I., Segschneider, J., & Wetzel, P. (2005). The Hamburg Ocean  
1312 Carbon Cycle Model HAMOCC5.1 - Technical Description Release 1.1. *Berichte zur*  
1313 *Erdsystemforschung*, *14*, 50 pp. (Max Planck Institute for Meteorology, Hamburg, Ger-  
1314 many)
- 1315 Marrec, P., Cariou, T., Macé, E., Morin, P., Salt, L. A., Vernet, M., ... Bozec, Y. (2015).  
1316 Dynamics of air-sea CO<sub>2</sub> fluxes in the northwestern European shelf based on voluntary  
1317 observing ship and satellite observations. *Biogeosciences*, *12*, 5371-5391. doi: 10.5194/  
1318 bg-12-5371-2015
- 1319 Marsaleix, P., Auclair, F., & Estournel, C. (2006). Considerations on Open Boundary  
1320 Conditions for Regional and Coastal Ocean Models. *Journal of Atmospheric and Oceanic*  
1321 *Technology*, *23*, 1604-1613. doi: 10.1175/JTECH1930.1
- 1322 Mathis, M., Elizalde, A., & Mikolajewicz, U. (2018). Which complexity of regional climate  
1323 system models is essential for downscaling anthropogenic climate change in the Northwest  
1324 European Shelf? *Climate Dynamics*, *50*, 2637-2659.
- 1325 Mathis, M., Elizalde, A., & Mikolajewicz, U. (2019). The future regime of Atlantic nutrient  
1326 supply to the Northwest European Shelf. *J. Mar. Syst.*, *189*, 98-115. doi: 10.1016/  
1327 j.jmarsys.2018.10.002
- 1328 Mathis, M., Elizalde, A., Mikolajewicz, U., & Pohlmann, T. (2015). Variability patterns of  
1329 the general circulation and sea water temperature in the North Sea. *Prog. Oceanog.*, *135*,  
1330 91-112.
- 1331 Mathis, M., Mayer, B., & Pohlmann, T. (2013). An uncoupled dynamical downscaling for  
1332 the North Sea: Method and evaluation. *Ocean Modelling*, *72*, 153-166.
- 1333 Mauritsen, T., Bader, J., Becker, T., Behrens, J., Bittner, M., Brokopf, R., ... Roeckner,

- 1334 E. (2019). Developments in the MPI-M Earth System Model version 1.2 (MPI-ESM1.2)  
 1335 and its response to increasing CO<sub>2</sub>. *Journal of Advances in Modeling Earth Systems*, *11*,  
 1336 998-1038. doi: 10.1029/2018MS001400
- 1337 Mayer, B., Rixen, T., & Pohlmann, T. (2018). The Spatial and Temporal Variability of  
 1338 Air-Sea CO<sub>2</sub> Fluxes and the Effect of Net Coral Reef Calcification in the Indonesian Seas:  
 1339 A Numerical Sensitivity Study. *Frontiers in Marine Science*, *5*, 19 pp. doi: 10.3389/  
 1340 fmars.2018.00116
- 1341 Meybeck, M. (1982). Carbon, Nitrogen, and Phosphorus Transport by World Rivers. *Am.*  
 1342 *J. Sci.*, *282*, 401-450. doi: 10.2475/ajs.282.4.401
- 1343 Meybeck, M., & Vörösmarty, C. (1999). Global Transfer of Carbon by Rivers. *Global*  
 1344 *Change Newsletters, IGBP Newsletter No. 37*, 18-19.
- 1345 Middelburg, J. J., Soetaert, K., & Hagens, M. (2020). Ocean Alkalinity, Buffering and  
 1346 Biogeochemical Processes. *Reviews of Geophysics*, *58*, e2019RG000681. doi: 10.1029/  
 1347 2019RG000681
- 1348 Moll, A. (1998). Regional distribution of primary production in the North Sea simulated  
 1349 by a three-dimensional model. *Journal of Marine Systems*, *16*, 151-170.
- 1350 Monteiro, T., Kerr, R., & da Costa Machado, E. (2020b). Seasonal variability of net sea-air  
 1351 CO<sub>2</sub> fluxes in a coastal region of the northern Antarctic Peninsula. *Sci. Rep.*, *10*, 15 pp.  
 1352 doi: 10.1038/s41598-020-71814-0
- 1353 Monteiro, T., Kerr, R., Orselli, I. B. M., & Lencina-Avila, J. M. (2020a). Towards an  
 1354 intensified summer CO<sub>2</sub> sink behaviour in the Southern Ocean coastal regions. *Prog.*  
 1355 *Oceanogr.*, *183*, 13 pp. doi: 10.1016/j.pocean.2020.102267
- 1356 Muller-Karger, F. E., Varela, R., Thunell, R. C., Luerssen, R., Hu, C., & Walsh, J. J. (2005).  
 1357 The importance of continental margins in the global carbon cycle. *Geophys. Res. Letters*,  
 1358 *32*, L01602. doi: 10.1029/2004GL021346
- 1359 Najjar, R. G., Jin, X., Louanchi, F., Aumont, O., Caldeira, K., Doney, S. C., ... Yool,  
 1360 A. (2007). Impact of circulation on export production, dissolved organic matter, and  
 1361 dissolved oxygen in the ocean: Results from Phase II of the Ocean Carbon-cycle Model  
 1362 Intercomparison Project (OCMIP-2). *Global Biogeochemical Cycles*, *21*, 22 p. doi: 10  
 1363 .1029/2006GB002857
- 1364 Nellemann, C., Corcoran, E., Duarte, C., Valdes, L., Young, C., Fonseca, L., & Grimsditch,  
 1365 G. (2009). Blue Carbon - The Role of Healthy Oceans in Binding Carbon. *A Rapid*  
 1366 *Response Assessment. United Nations Environment Programme.*
- 1367 Oguz, T., Macias, D., , & Tintore, J. (2015). Ageostrophic frontal processes controlling  
 1368 phytoplankton production in the Catalano-Balearic Sea (Western Mediterranean). *PLoS*  
 1369 *One*, *10*, 22 pp. doi: 10.1371/journal.pone.0129045
- 1370 O'Meara, T., Gibbs, E., & Thrush, S. F. (2018). Rapid organic matter assay of organic  
 1371 matter degradation across depth gradients within marine sediments. *Methods Ecol. Evol.*,  
 1372 *9*, 245-253. doi: 10.1111/2041-210X.12894
- 1373 Pain, C. C., Piggott, M. D., Goddard, A. J. H., Fang, F., Gorman, G. J., Marshall, D. P.,  
 1374 ... de Oliveira, C. R. E. (2005). Three-dimensional unstructured mesh ocean modelling.  
 1375 *Ocean Modelling*, *10*, 5-33. doi: 10.1016/j.ocemod.2004.07.005
- 1376 Painter, S. C., Hartman, S. E., Kivimäe, C., Salt, L. A., Clargo, N. M., Bozec, Y., ...  
 1377 Allen, S. R. (2016). Carbon exchange between a shelf sea and the ocean: The Hebrides  
 1378 Shelf, west of Scotland. *Journal of Geophysical Research: Oceans*, *121*, 4522-4544. doi:  
 1379 10.1002/2015JC011599
- 1380 Painting, S. J., Collingridge, K. A., Durand, D., Grémare, A., Créach, V., Arvanitidis, C., &  
 1381 Bernard, G. (2020). Marine monitoring in Europe: is it adequate to address environmental  
 1382 threats and pressures? *Ocean Sci.*, *16*, 235-252. doi: 10.5194/os-16-235-2020
- 1383 Palastanga, V., Slomp, C. P., & Heinze, C. (2011). Long-term controls on ocean phosphorus  
 1384 and oxygen in a global biogeochemical model. *Global Biogeochemical Cycles*, *25*, 19 pp.  
 1385 doi: 10.1029/2010GB003827
- 1386 Park, G. H., Wanninkhof, R., Doney, S. C., Takahashi, T., Lee, K., Feely, R. A., ... Lima,  
 1387 I. (2010). Variability of global air-sea CO<sub>2</sub> fluxes over the last three decades. *Tellus*,

- 1388       62B, 352-368. doi: 10.1111/j.1600-0889.2010.00498.x
- 1389       Pätsch, J., Burchard, H., Dieterich, C., Gräwe, U., Gröger, M., Mathis, M., ... Eden, C.  
1390       (2017). An evaluation of the North Sea circulation in global and regional models relevant  
1391       for ecosystem simulations. *Ocean Modelling*, *116*, 70-95.
- 1392       Paulsen, H., Ilyina, T., Six, K. D., & Stemmler, I. (2017). Incorporating a prognostic repre-  
1393       sentation of marine nitrogen fixers into the global ocean biogeochemical model HAMOCC.  
1394       *Journal of Advances in Modeling Earth Systems*, *9*, 438-464. doi: 10.1002/2016MS000737
- 1395       Piggott, M. D., Pain, C. C., Gorman, G. J., Marshall, D. P., & Killworth, P. D. (2008).  
1396       Unstructured Adaptive Meshes for Ocean Modeling. In M. W. Hecht & H. Hasumi (Eds.),  
1397       *Ocean modeling in an eddying regime* (p. 383-408). American Geophysical Union (AGU).  
1398       doi: 10.1029/177GM22
- 1399       Pimenta, F. M., Campos, E. J. D., Miller, J. L., & Piola, A. R. (2005). A numerical study  
1400       of the Plata River plume along the southeastern South American continental shelf. *Braz.*  
1401       *J. Oceanogr.*, *53*, 129-146.
- 1402       Piola, A. R., Palma, E. D., Bianchi, A. A., Castro, B. M., Dottori, M., Guerrero, R. A., ...  
1403       Saraceno, M. (2018). Physical Oceanography of the SW Atlantic Shelf: A Review. In  
1404       M. Hoffmeyer, M. Sabatini, F. Brandini, D. Calliari, & S. N. (Eds.), *Plankton Ecology of*  
1405       *the Southwestern Atlantic* (p. 37-56). Springer, Cham. doi: 10.1007/978-3-319-77869-3\_2
- 1406       Poulain, P. M., & Centurioni, L. (2015). Direct measurements of World Ocean tidal cur-  
1407       rents with surface drifters. *J. Geophys. Res. Oceans*, *120*, 6986-7003. doi: 10.1002/  
1408       2015JC010818
- 1409       Provoost, P., Braeckman, U., van Gansbeke, D., Moodley, L., Soetaert, K., Middelburg,  
1410       J. J., & Vanaverbeke, J. (2013). Modelling benthic oxygen consumption and benthic-  
1411       pelagic coupling at a shallow station in the southern North Sea. *Estuarine, Coastal and*  
1412       *Shelf Science*, *120*, 1-11. doi: 10.1016/j.ecss.2013.01.008
- 1413       Provoost, P., van Heuven, S., Soetaert, K., Laane, R. W. P. M., & Middelburg, J. J. (2010).  
1414       Seasonal and long-term changes in pH in the Dutch coastal zone. *Biogeosciences*, *7*,  
1415       3869-3878. doi: 10.5194/bg-7-3869-2010
- 1416       Quante, M., Colijn, F., Bakker, J. P., Härdtle, W., Heinrich, H., Lefebvre, C., ... Tölle,  
1417       M. H. (2016). Introduction to the Assessment - Characteristics of the Region. In  
1418       M. Quante & F. Colijn (Eds.), *North Sea Region Climate Change Assessment* (p. 175-  
1419       217). Springer Berlin - Heidelberg.
- 1420       Regnier, P., Friedlingstein, P., Ciais, P., Mackenzie, F. T., Gruber, N., Janssens, I. A., ...  
1421       Thullner, M. (2013). Anthropogenic perturbation of the carbon fluxes from land to ocean.  
1422       *Nature Geoscience*, *6*, 597-607. doi: 10.1038/ngeo1830
- 1423       Remacle, J. F., & Lambrechts, J. (2018). Fast and robust mesh generation on the sphere -  
1424       Application to coastal domains. *Computer-Aided Design*, *103*, 14-23. (25th International  
1425       Meshing Roundtable Special Issue: Advances in Mesh Generation) doi: 10.1016/j.cad  
1426       .2018.03.002
- 1427       Resplandy, L., Keeling, R. F., Rödenbeck, C., Stephens, B. B., Khatiwala, S., Rodgers,  
1428       K. B., ... Tans, P. P. (2018). Revision of global carbon fluxes based on a reassessment  
1429       of oceanic and riverine carbon transport. *Nat. Geosci.*, *11*, 504-509. doi: 10.1038/  
1430       s41561-018-0151-3
- 1431       Reynaud, J. Y., & Dalrymple, R. (2012). Shallow-Marine Tidal Deposits. In R. A. J. Davis &  
1432       R. W. Dalrymple (Eds.), *Principles of tidal sedimentology* (p. 335-369). Springer Science  
1433       and Business Media B. V. doi: 10.1007/978-94-007-0123-6\_13
- 1434       Ridgwell, A. J., Watson, A. J., & Archer, D. E. (2002). Modeling the response of the  
1435       oceanic Si inventory to perturbation, and consequences for atmospheric CO<sub>2</sub>. *Global*  
1436       *Biogeochemical Cycles*, *16*, 26 pp. doi: 10.1029/2002GB001877
- 1437       Rippeth, T. P., Lincoln, B. J., Kennedy, H. A., Palmer, M. R., Sharples, J., & Williams,  
1438       C. A. J. (2014). Impact of vertical mixing on sea surface pCO<sub>2</sub> in temperate sea-  
1439       sonally stratified shelf seas. *J. Geophys. Res. Oceans*, *119*, 3868-3882. doi: 10.1002/  
1440       2014JC010089
- 1441       Roobaert, A., Laruelle, G. G., Landschützer, P., Gruber, N., Chou, L., & Regnier, P. (2019).

- 1442 The spatiotemporal dynamics of the sources and sinks of CO<sub>2</sub> in the global coastal ocean.  
1443 *Global Biogeochemical Cycles*, *33*, 1693-1714. doi: 10.1029/2019GB006239
- 1444 Schartau, M., Riethmüller, R., Flöser, G., van Beusekom, J. E. E., Krasemann, H., Hofmeister,  
1445 R., & Wirtz, K. (2019). On the separation between inorganic and organic fractions  
1446 of suspended matter in a marine coastal environment. *Progress in Oceanography*, *171*,  
1447 231-250. doi: 10.1016/j.pocean.2018.12.011
- 1448 Schmidt, S., Neumann, B., Waweru, Y., Durussel, C., Unger, S., & Visbeck, M. (2017).  
1449 SDG14 Conserve and Sustainably Use the Oceans, Seas and Marine Resources for Sus-  
1450 tainable Development. In D. J. Griggs, M. Nilsson, A. Stevance, & D. McCollum (Eds.),  
1451 *A guide to sdg interactions: from science to implementation* (p. 174-218). International  
1452 Council for Science (ICSU), Paris. doi: 10.24948/2017.01
- 1453 Séférian, R., Berthet, S., Yool, A., Palmiéri, J., Bopp, L., Tagliabue, A., ... Yamamoto,  
1454 A. (2020). Tracking Improvement in Simulated Marine Biogeochemistry Between CMIP5  
1455 and CMIP6. *Curr. Clim. Change Rep.*, *6*, 95-119. doi: 10.1007/s40641-020-00160-0
- 1456 Sein, D., Mikolajewicz, U., Gröger, M., Fast, I., Cabos, I., Pinto, J., ... Jacob, D. (2015).  
1457 Regionally coupled atmosphere-ocean-sea ice-marine biogeochemistry model ROM. Part  
1458 I: Description and validation. *J. Adv. Model. Earth Syst.*, *7*, 268-304.
- 1459 Sein, D. V., Koldunov, N. V., Danilov, S., Wang, Q., Sidorenko, D., Fast, I., ... Jung, T.  
1460 (2017). Ocean modeling on a mesh with resolution following the local Rossby radius. *Jour-  
1461 nal of Advances in Modeling Earth Systems*, *9*, 2601-2614. doi: 10.1002/2017MS001099
- 1462 Seitzinger, S. P., Mayorga, E., Bouwman, A. F., Kroeze, C., Beusen, A. H. W., Billen, G.,  
1463 ... Harrison, J. A. (2010). Global river nutrient export: A scenario analysis of past and  
1464 future trends. *Global Biogeochemical Cycles*, *24*, 16 pp. doi: 10.1029/2009GB003587
- 1465 Simmons, H. L., Jayne, S. R., St. Laurent, L. C., & Weaver, A. J. (2004). Tidally driven  
1466 mixing in a numerical model of the ocean general circulation. *Ocean Modelling*, *6*, 245-  
1467 263. doi: 10.1016/S1463-5003(03)00011-8
- 1468 Six, K. D., & Maier-Reimer, E. (1996). Effects of plankton dynamics on seasonal carbon  
1469 fluxes in an ocean general circulation model. *Global Biogeochem. Cycles*, *10*, 559-583.
- 1470 Song, J., Qu, B., Li, X., Yuan, H., Li, N., & Duan, L. (2018). Carbon sinks/sources in  
1471 the Yellow and East China Seas - Air-sea interface exchange, dissolution in seawater,  
1472 and burial in sediments. *Science China Earth Sciences*, *61*, 1583-1593. doi: 10.1007/  
1473 s11430-017-9213-6
- 1474 Stuhne, G. R., & Peltier, W. R. (2009). An unstructured C-grid based method for 3-D  
1475 global ocean dynamics: Free-surface formulations and tidal test cases. *Ocean Modelling*,  
1476 *28*, 97-105. doi: 10.1016/j.ocemod.2008.11.005
- 1477 Su, J., Tian, T., Krasemann, H., Schartau, M., & Wirtz, K. (2015). Response patterns  
1478 of phytoplankton growth to variations in resuspension in the German Bight revealed by  
1479 daily MERIS data in 2003 and 2004. *Oceanologia*, *57*, 328-341. doi: 10.1016/j.oceano  
1480 .2015.06.001
- 1481 Sündermann, J., & Pohlmann, T. (2011). A brief analysis of North Sea physics. *Oceanologia*,  
1482 *53*(3), 663-689.
- 1483 Takahashi, T., Sutherland, S. C., Sweeney, C., Poisson, A., Metzl, N., Tilbrook, B., ...  
1484 Nojiri, Y. (2002). Global sea-air CO<sub>2</sub> flux based on climatological surface ocean pCO<sub>2</sub>,  
1485 and seasonal biological and temperature effects. *Deep Sea Research Part II: Topical  
1486 Studies in Oceanography*, *49*, 1601-1622. doi: 10.1016/S0967-0645(02)00003-6
- 1487 Tamburini, F., & Föllmi, K. B. (2009). Phosphorus burial in the ocean over glacial-  
1488 interglacial time scales. *Biogeosciences*, *6*, 501-513. doi: 10.5194/bg-6-501-2009
- 1489 Tan, S., & Shi, G. (2006). Satellite-derived primary productivity and its spatial and temporal  
1490 variability in the China seas. *Journal of Geographical Sciences*, *16*, 447-457. doi: 10.1007/  
1491 s11442-006-0408-4
- 1492 Tan, S., & Shi, G. (2012). The relationship between satellite-derived primary production and  
1493 vertical mixing and atmospheric inputs in the Yellow Sea cold water mass. *Continental  
1494 Shelf Research*, *48*, 138-145. doi: 10.1016/j.csr.2012.07.015
- 1495 Taylor, K., Stouffer, R. J., & Meehl, G. A. (2012). An overview of CMIP5 and the experiment

- 1496 design. *Bull. Am. Meteorol. Soc.*, *93*, 485-498. doi: 10.1175/BAMS-D-11-00094.1
- 1497 Thévenin, M. R., Pereira, J., & Lessa, G. C. (2019). Shelf-break upwelling on a very  
1498 narrow continental shelf adjacent to a western boundary current formation zone. *Journal*  
1499 *of Marine Systems*, *194*, 52-65. doi: 10.1016/j.jmarsys.2019.02.008
- 1500 Thomas, H., Bozec, Y., Elkalay, K., & de Baar, H. J. W. (2004). Enhanced Open Ocean  
1501 Storage of CO<sub>2</sub> from Shelf Sea Pumping. *Science*, *304*(5673), 1005-1008.
- 1502 Toffoli, A., & Bitner-Gregersen, E. M. (2017). Types of Ocean Surface Waves, Wave  
1503 Classification. In J. Carlton, P. Jukes, & Y. Choo (Eds.), *Encyclopedia of maritime and*  
1504 *offshore engineering* (p. 1-8). John Wiley & Sons, Ltd. doi: 10.1002/9781118476406  
1505 .emoe077
- 1506 Tréguer, P. J., & De La Rocha, C. L. (2013). The World Ocean Silica Cycle. *Annual Review*  
1507 *of Marine Science*, *5*, 477-501. doi: 10.1146/annurev-marine-121211-172346
- 1508 Tréguer, P. J., Sutton, J. N., Brzezinski, M., Charette, M. A., Devries, T., Dutkiewicz, S.,  
1509 ... Rouxel, O. (2021). Reviews and syntheses: The biogeochemical cycle of silicon in the  
1510 modern ocean. *Biogeosciences*, *18*, 1269-1289. doi: 10.5194/bg-18-1269-2021
- 1511 Tseng, C. M., Liu, K. K., Gong, G. C., Shen, P. Y., & Cai, W. J. (2011). CO<sub>2</sub> uptake in the  
1512 East China Sea relying on Changjiang runoff is prone to change. *Geophysical Research*  
1513 *Letters*, *38*, 6 pp. doi: 10.1029/2011GL049774
- 1514 van Cappellen, P., Dixit, S., & van Beusekom, J. (2002). Biogenic silica dissolution in the  
1515 oceans: Reconciling experimental and field-based dissolution rates. *Global Biogeochemical*  
1516 *Cycles*, *16*, 10 pp. doi: 10.1029/2001GB001431
- 1517 van Leeuwen, S., Tett, P., Mills, D., & van der Molen, J. (2015). Stratified and nonstratified  
1518 areas in the North Sea: Long-term variability and biological and policy implications. *J.*  
1519 *Geophys. Res. Oceans*, *120*, 4670-4686. doi: 10.1002/2014JC010485
- 1520 Vantrepotte, V., Loisel, H., Dessailly, D., & Mériaux, X. (2012). Optical classification of  
1521 contrasted coastal waters. *Remote Sensing of Environment*, *123*, 306-323. doi: 10.1016/  
1522 j.rse.2012.03.004
- 1523 Violante, R. A., Paterlini, C. M., Marcolini, S. I., Costa, I. P., Cavallotto, J. L., Laprida, C.,  
1524 ... Osterrieth, M. L. (2014). The Argentine continental shelf: Morphology, sediments,  
1525 processes and evolution since the last glacial maximum. *Geological Society Memoir*, *41*,  
1526 55-68. doi: 10.1144/M41.6
- 1527 Volk, T., & Hoffert, M. I. (1985). Ocean Carbon Pumps: Analysis of Relative Strengths and  
1528 Efficiencies in Ocean-Driven Atmospheric CO<sub>2</sub> Changes. In E. Sundquist & W. Broecker  
1529 (Eds.), *The carbon cycle and atmospheric CO<sub>2</sub>: Natural variations from the present to the future*  
1530 (p. 99-110). American Geophysical Union (AGU). doi: 10.1029/GM032p0099
- 1531 Wallmann, K. (2010). Phosphorus imbalance in the global ocean? *Global Biogeochem.*  
1532 *Cycles*, *24*, 12 pp. doi: 10.1029/2009GB003643
- 1533 Ward, N. D., Bianchi, T. S., Medeiros, P. M., Seidel, M., Richey, J. E., Keil, R. G., &  
1534 Sawakuchi, H. O. (2017). Where Carbon Goes When Water Flows: Carbon Cycling  
1535 across the Aquatic Continuum. *Frontiers in Marine Science*, *4*, 27 pp. doi: 10.3389/  
1536 fmars.2017.00007
- 1537 Ward, N. D., Megonigal, J. P., Bond-Lamberty, B., Bailey, V. L., Butman, D., Canuel,  
1538 E. A., ... Windham-Myers, L. (2020). Representing the function and sensitivity of  
1539 coastal interfaces in Earth system models. *Nature Communications*, *11*, 14 pp. doi:  
1540 10.1038/s41467-020-16236-2
- 1541 Weller, H., Browne, P., Budd, C., & Cullen, M. (2016). Mesh adaptation on the sphere  
1542 using optimal transport and the numerical solution of a Monge-Ampère type equation.  
1543 *Journal of Computational Physics*, *308*, 102-123. doi: 10.1016/j.jcp.2015.12.018
- 1544 Williams, C., Sharples, J., Mahaffey, C., & Rippeth, T. (2013). Wind-driven nutrient pulses  
1545 to the subsurface chlorophyll maximum in seasonally stratified shelf seas. *Geophysical*  
1546 *Research Letters*, *40*, 1-6. doi: 10.1002/2013GL058171
- 1547 Wilson, R. J., & Heath, M. R. (2019). Increasing turbidity in the North Sea during  
1548 the 20th century due to changing wave climate. *Ocean Science*, *15*, 1615-1625. doi:  
1549 10.5194/os-15-1615-2019

- 1550 Wu, R., Lin, J., & Li, B. (2016). Spatial and Temporal Variability of Sea Surface Tem-  
 1551 perature in Eastern Marginal Seas of China. *Advances in Meteorology*, 2016, 1-9. doi:  
 1552 10.1155/2016/3820720
- 1553 Xie, F., Tao, Z., Zhou, X., Lv, T., & Wang, J. (2019). Spatial and Temporal Variations  
 1554 of Particulate Organic Carbon Sinking Flux in Global Ocean from 2003 to 2018. *Remote*  
 1555 *Sens.*, 11, 20 pp. doi: 10.3390/rs11242941
- 1556 Yang, S., Song, B., Ye, S., Laws, E., He, L., Li, J., ... Behling, H. (2019). Large-scale  
 1557 pollen distribution in marine surface sediments from the Bohai Sea, China: Insights into  
 1558 pollen provenance, transport, deposition, and coastal-shelf paleoenvironment. *Progress in*  
 1559 *Oceanography*, 178, 17 pp. doi: 10.1016/j.pocean.2019.102183
- 1560 Yang, S., Wang, Z., Dou, Y., & Shi, X. (2014). A review of sedimentation since the Last  
 1561 Glacial Maximum on the continental shelf of eastern China. *Geological Society, London,*  
 1562 *Memoirs*, 41, 293-303. doi: 10.1144/M41.21
- 1563 Yao, Z., He, R., Bao, X., Wu, D., & Song, J. (2012). M2 tidal dynamics in Bohai and  
 1564 Yellow Seas: a hybrid data assimilative modeling study. *Ocean Dynamics*, 62, 753-769.  
 1565 doi: 10.1007/s10236-011-0517-1
- 1566 Yasunaka, S., Murata, A., Watanabe, E., Chierici, M., Fransson, A., van Heuven, S., ...  
 1567 Wanninkhof, R. (2016). Mapping of the air-sea CO<sub>2</sub> flux in the Arctic Ocean and its  
 1568 adjacent seas: Basin-wide distribution and seasonal to interannual variability. *Polar*  
 1569 *Science*, 10, 323-334. doi: 10.1016/j.polar.2016.03.006
- 1570 Yasunaka, S., Siswanto, E., Olsen, A., Hoppema, M., Watanabe, E., Fransson, A., ...  
 1571 Mathis, J. T. (2018). Arctic Ocean CO<sub>2</sub> uptake: an improved multiyear estimate of the  
 1572 air-sea CO<sub>2</sub> flux incorporating chlorophyll *a* concentrations. *Biogeosciences*, 15, 1643-  
 1573 1661. doi: 10.5194/bg-15-1643-2018
- 1574 Yuan, D., Zhu, J., Li, C., & Hu, D. (2008). Cross-shelf circulation in the Yellow and East  
 1575 China Seas indicated by MODIS satellite observations. *Journal of Marine Systems*, 70,  
 1576 134-149. doi: 10.1016/j.jmarsys.2007.04.002
- 1577 Yvon-Durocher, G., Caffrey, J. M., Cescatti, A., Dossena, M., del Giorgio, P., Gasol, J. M.,  
 1578 ... Allen, A. P. (2012). Reconciling the temperature dependence of respiration across  
 1579 timescales and ecosystem types. *Nature*, 487, 472-476. doi: 10.1038/nature11205
- 1580 Zhao, C., Daewel, U., & Schrum, C. (2019). Tidal impacts on primary production in the  
 1581 North Sea. *Earth Syst. Dynam.*, 10, 287-317. doi: 10.5194/esd-10-287-2019
- 1582 Zhou, Y., Evans, C., Chen, Y., Chang, K., & Martin, P. (2021). Extensive remineralization  
 1583 of peatland-derived dissolved organic carbon and acidification in the Sunda Shelf Sea,  
 1584 Southeast Asia. *Earth and Space Science Open Archive*, 67 pp. doi: 10.1002/essoar  
 1585 .10506636.1
- 1586 Zhu, J., Wu, H., & Li, L. (2015). Hydrodynamics of the Changjiang Estuary and Adja-  
 1587 cent Seas. In J. Zhang (Ed.), *Ecological continuum from the changjiang (yangtze river)*  
 1588 *watersheds to the east china sea continental margin* (p. 19-45). Springer International  
 1589 Publishing Switzerland. doi: 10.1007/978-3-319-16339-0\_2
- 1590 Zweng, M. M., Reagan, J. R., Antonov, J. I., Locarnini, R. A., Mishonov, A. V., Boyer,  
 1591 T. P., ... Biddle, M. M. (2013). World Ocean Atlas 2013, Volume 2: Salinity. *Levitus,*  
 1592 *S., Mishonov, A. (Eds.), NOAA Atlas NESDIS, 74*, 39 pp.